2010-04

Parametrizing turbulent exchange over summer sea ice and the marginal ice zone

Andreas, Edgar L.

Andreas EL, Horst TW, Grachev AA, Persson POG, Fairall CW, Guest PS, Jordan RE. 2010. Parametrizing turbulent exchange over summer sea ice and themarginal ice zone. Q. J. R. þÿ M e t e o r o l . S o c . 1 3 6 : 9 2 7 9 4 3 . D O I : 1 0 . 1 0 0 2 / q j . 6 1 8

RMetS
Royal Meteorological Society

Parametrizing turbulent exchange over summer sea ice and the marginal ice zone

Edgar L Andreas,[a*] Thomas W. Horst,[b] Andrey A. Grachev,[c,d] P. Ola G. Persson,[c,d] Christopher W. Fairall,[c†] Peter S. Guest[e†] and Rachel E. Jordan[f]

[a]*NorthWest Research Associates, Inc., Lebanon, New Hampshire, USA*
[b]*National Center for Atmospheric Research, Boulder, Colorado, USA*
[c]*NOAA Earth System Research Laboratory, Boulder, Colorado, USA*
[d]*Cooperative Institute for Research in Environmental Sciences, University of Colorado, Boulder, Colorado, USA*
[e]*Naval Postgraduate School, Monterey, California, USA*
[f]*Jordan Environmental Modeling, PC, Hanover, New Hampshire, USA*
*Correspondence to: Edgar L Andreas, NorthWest Research Associates, Inc., (Seattle Division), 25 Eagle Ridge, Lebanon, New Hampshire 03766-1900, USA. E-mail: eandreas@nwra.com
†The contributions of Christopher W. Fairall and Peter S. Guest to this article were prepared as part of their official duties as United States Federal Government employees.

The surface of the Arctic Ocean in summer is a mix of sea ice and water in both leads and melt ponds. Here we use data collected at multiple sites during the year-long experiment to study the Surface Heat Budget of the Arctic Ocean (SHEBA) to develop a bulk turbulent flux algorithm for predicting the surface fluxes of momentum and sensible and latent heat over the Arctic Ocean during summer from readily measured or modelled quantities. The distinctive aerodynamic feature of summer sea ice is that the leads and melt ponds create vertical ice faces that the wind can push against; momentum transfer to the surface is thus enhanced through form drag. In effect, summer sea ice behaves aerodynamically like the marginal ice zone, which is another surface that consists of sea ice and water. In our bulk flux algorithm, we therefore combine our SHEBA measurements of the neutral-stability drag coefficient at a reference height of 10 m, C_{DN10}, with similar measurements from marginal ice zones that have been reported in the literature to create a unified parametrization for C_{DN10} for summer sea ice and for any marginal ice zone. This parametrization predicts C_{DN10} from a second-order polynomial in ice concentration. Our bulk flux algorithm also includes expressions for the roughness lengths for temperature and humidity, introduces new profile stratification corrections for stable stratification, and effectively eliminates the singularities that often occur in iterative flux algorithms for very light winds. In summary, this new algorithm seems capable of estimating the friction velocity u_* (a surrogate for the momentum flux) over summer sea ice with an absolute accuracy of 0.02–0.03 m s^{-1}; the sensible heat flux, with an accuracy of about 6 W m^{-2}; and the latent heat flux, with an accuracy of 3.5 W m^{-2}. Copyright © 2010 Royal Meteorological Society

Key Words: Arctic Ocean; bulk turbulent flux algorithm; drag coefficient; fictitious correlation; Monin-Obukhov similarity; roughness lengths; SHEBA; turbulence measurements

Received 17 September 2009; Revised 25 January 2010; Accepted 1 March 2010; Published online in Wiley InterScience 30 April 2010

Citation: Andreas EL, Horst TW, Grachev AA, Persson POG, Fairall CW, Guest PS, Jordan RE. 2010. Parametrizing turbulent exchange over summer sea ice and the marginal ice zone. *Q. J. R. Meteorol. Soc.* **136**: 927–943. DOI:10.1002/qj.618

1. Introduction

In the height of summer, the surface of the Arctic Ocean comprises sea ice and open water in leads and melt ponds. In effect, the leads and melt ponds create vertical sea-ice faces that the wind can push against (Figure 1). As a result, turbulent momentum transfer at the surface is enhanced because it now arises through a combination of skin friction at the horizontal surfaces and form drag associated with the (nearly) vertical surfaces.

During SHEBA, the year-long experiment in 1997 and 1998 to study the Surface Heat Budget of the Arctic Ocean (Uttal *et al.*, 2002), our Atmospheric Surface Flux Group (ASFG) evaluated the neutral-stability drag coefficient at a 10 m reference height, C_{DN10}, hourly at multiple sites over sea ice for nearly a year. Figure 2 shows the time series of these C_{DN10} values and the fractional surface coverage of water in leads and melt ponds.

On the basis of this plot, we divided the SHEBA year into just two aerodynamic seasons: winter and summer. In winter, the sea ice was compact, visually uniform, and snow covered; and the snow was dry enough and deep enough to drift and blow under wind forcing. In summer, in contrast, the snow was too wet and sticky to drift and eventually melted and disappeared. Furthermore, leads opened and melt ponds formed; at the height of summer, the surface around the SHEBA camp was about 60% bare ice and about 40% water. During SHEBA, aerodynamic summer ran from 15 May to 14 September 1998. Winter constituted the first half and the last couple of weeks of our SHEBA deployment.

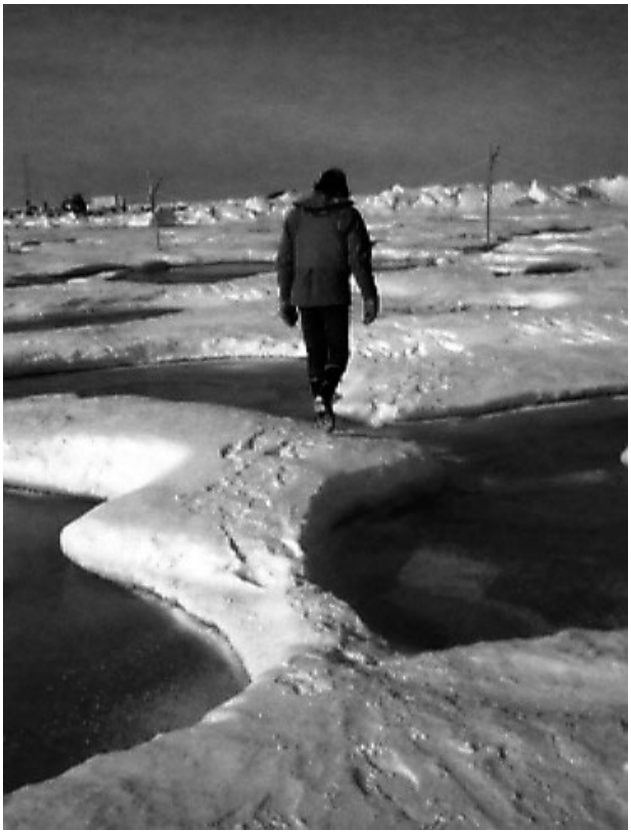

Figure 1. Melt ponds near the SHEBA ice camp in early August 1998. Photo by Tony Beesley

An interesting feature of the C_{DN10} series in Figure 2 is that, during winter (especially the left half of the series), the C_{DN10} values are somewhat scattered although the sea ice surface appeared visually homogeneous. In summer (May–September in Figure 2), in contrast, although the surface appeared quite heterogeneous, the C_{DN10} values collapse to a common trend that mirrors the evolution of the water fraction. We infer that the form drag fostered by the vertical ice faces enhanced the turbulent mixing and, therefore, tended to homogenise the atmospheric surface layer in summer.

One of the goals of our participation in SHEBA was to develop a bulk flux algorithm (cf. Fairall *et al.*, 1996, 2003) to accurately predict the turbulent surface fluxes of momentum and sensible and latent heat. Here we describe our bulk flux algorithm for summer sea ice. Andreas *et al.* (2003, 2005b) report our preliminary work on this algorithm. Andreas *et al.* (2010) describe our companion bulk flux algorithm for winter sea ice. Brunke *et al.* (2006) give alternative flux algorithms for both summer and winter based on this same SHEBA dataset; but our approach differs significantly from theirs. First, we acknowledge the contributions of form drag on the parametrization for momentum transfer in summer; and second, our analysis minimises the effects of fictitious correlation that, we believe (Andreas *et al.*, 2010), influenced the analyses by Brunke *et al.*.

We base our bulk flux algorithm on Monin–Obukhov similarity theory. Using data from our main 20 m SHEBA tower, Grachev *et al.* (2007a, 2007b) developed new wind speed and scalar profile similarity functions to specifically treat the very stable stratification that we encountered during SHEBA. We include those new functions in our flux algorithm.

Another essential feature of a bulk flux algorithm is a module that predicts the roughness length for wind speed (z_0) or, equivalently, C_{DN10}. Morphologically, the

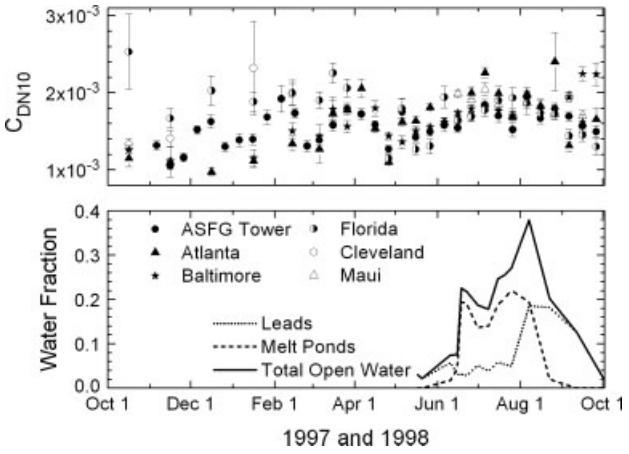

Figure 2. The upper panel is the 10 m, neutral-stability drag coefficient obtained from hourly eddy-covariance measurements at six SHEBA sites: our main Atmospheric Surface Flux Group (ASFG) tower and five portable automated mesonet (PAM) sites named Atlanta, Baltimore, Cleveland, Florida and Maui. Symbols represent averages of all good hourly data collected during the first 10 days of the month, the second 10 days of the month, and the final 8, 10, or 11 days of the month. Error bars represent two standard deviations in the average. This plot summarises over 18 500 hours of data. The lower panel shows the fractional surface area of open water in leads, in melt ponds, and the sum of the two during summer. The water fraction data were obtained from aerial photographs taken during periodic, 200 km long helicopter surveys around the SHEBA ice camp (Perovich *et al.*, 2002)

marginal ice zone is like summer sea ice: The surface consists of significant areas of both ice and water (e.g. Guest and Davidson, 1987, 1991), and form drag is presumed to crucially influence surface momentum exchange (e.g. Andreas *et al.*, 1984; Birnbaum and Lüpkes, 2002). We noticed that measurements of C_{DN10} in marginal ice zones link nicely with our measurements of C_{DN10} over summer sea ice and, therefore, develop a unified parametrization of C_{DN10} for both summer sea ice and marginal ice zones that is a function of just ice concentration.

Yet another module in a bulk flux algorithm must predict the roughness lengths for temperature (z_T) and humidity (z_Q). Our data show that the ratios z_T/z_0 and z_Q/z_0 as functions of the roughness Reynolds number, $R_* = u_* z_0/\nu$, where u_* is the friction velocity and ν is the kinematic viscosity of air, follow Andreas's (1987) theoretical model. Plots of these quantities, however, are prone to fictitious correlation if measured values are used throughout to test Andreas's model (Andreas, 2002; Andreas *et al.*, 2010). We circumvent this problem by using data to compute z_T/z_0 and z_Q/z_0 but using our bulk flux algorithm to compute R_*.

2. Bulk flux algorithm

Energy budget studies or atmospheric models with sea ice as the lower boundary almost always estimate the surface fluxes of momentum (τ) and sensible (H_s) and latent (H_L) heat from a bulk flux algorithm (e.g. Maykut, 1978; Ebert and Curry, 1993: Jordan *et al.*, 1999; Briegleb *et al.*, 2004; Huwald *et al.*, 2005). In our algorithm, the relevant flux equations take the form

$$\tau = -\rho\,\overline{uw} \;\equiv\; \rho\,u_*^2 = \rho\,C_{Dr}\,S_r^2, \tag{2.1a}$$

$$H_{\mathrm{s}} = \rho\,c_p\overline{w\theta} = \;\rho\;\; c_p\,C_{Hr}\,S_r\,(\Theta_s - \Theta_r), \tag{2.1b}$$

$$H_{\mathrm{L}} = \rho\,L_{\mathrm{v}}\overline{wq} = \rho\,L_{\mathrm{v}}\,C_{Er}\,S_r\,(Q_s - Q_r). \tag{2.1c}$$

In these, u, w, θ, and q are turbulent fluctuations in longitudinal wind speed, vertical wind speed, temperature, and specific humidity; the overbar indicates a time average. Also, ρ is the air density; c_p, the specific heat of air at constant pressure; L_{v}, the latent heat of sublimation; S_r, the effective wind speed at reference height r; Θ_r and Q_r, the potential temperature and specific humidity at r; and Θ_s and Q_s, the temperature and specific humidity at the surface. We evaluate Q_s as the saturation value at Θ_s. See Andreas (2005) for the functions we use for calculating quantities like ρ, c_p, L_{v}, and Q_s. Equation (2.1a) also defines the friction velocity, u_*, which we use henceforth as a surrogate for the momentum flux.

The crux of any bulk flux algorithm is evaluating the transfer coefficients for momentum, sensible heat, and latent heat appropriate for height r – respectively, C_{Dr}, C_{Hr}, and C_{Er} in (2.1). These generally derive from Monin–Obukhov similarity theory and formally are (e.g. Garratt, 1992, p 52 ff.; Andreas, 1998)

$$C_{Dr} = \frac{k^2}{\{\ln(r/z_0) - \psi_m(r/L)\}^2}, \tag{2.2a}$$

$$C_{Hr} = \frac{k^2}{\{\ln(r/z_0) - \psi_m(r/L)\}\{\ln(r/z_T) - \psi_h(r/L)\}}, \tag{2.2b}$$

$$C_{Er} = \frac{k^2}{\{\ln(r/z_0) - \psi_m(r/L)\}\{\ln(r/z_Q) - \psi_h(r/L)\}}. \tag{2.2c}$$

In these, k (= 0.40) is the von Kármán constant, and ψ_m and ψ_h are empirical functions of the Obukhov length,

$$L = -\frac{\overline{\Theta_{\mathrm{v}}}}{k\,g}\left(\frac{u_*^3}{\overline{w\theta_{\mathrm{v}}}}\right) = -\frac{\overline{\Theta}}{k\,g}\left(\frac{u_*^3}{\overline{w\theta} + \frac{0.61\overline{\Theta}}{1+0.61\overline{Q}}\overline{wq}}\right). \tag{2.3}$$

Here, g is the acceleration of gravity; $\overline{\Theta}$, $\overline{\Theta_{\mathrm{v}}}$, and $\overline{Q}$ are surface-layer averages of the air temperature, virtual temperature, and specific humidity; and $\overline{w\theta_{\mathrm{v}}}$ is the flux of virtual temperature.

For the stratification corrections ψ_m and ψ_h in (2.2), we use Paulson's functions (1970) in unstable stratification and the functions from Grachev *et al.* (2007a) in stable stratification. These latter functions are based on our SHEBA tower data and include proper treatment of a heretofore unrecognised scaling regime in very stable stratification. The z_0, z_T, and z_Q in (2.2) are the roughness lengths for wind speed, temperature, and humidity, respectively.

Finally, S_r in (2.1) is an effective wind speed. For compatibility with the Coupled Ocean–Atmosphere Response Experiment (COARE) algorithm (Fairall *et al.*, 1996, 2003) and other recent flux algorithms (e.g. Andreas *et al.*, 2008), we acknowledge that in unstable stratification gustiness enhances turbulent exchange and therefore model

$$S_r = (U_r^2 + \beta_g^2 w_*^2)^{1/2}. \tag{2.4}$$

Here, U_r is the actual measured or modelled mean magnitude of the vector wind at reference height r, $\beta_g = 1.25$ (Fairall *et al.*, 1996), and w_* is Deardorff's (1970) convective velocity scale (Godfrey and Beljaars, 1991):

$$w_* = u_*\left(-\frac{z_i}{k\,L}\right)^{1/3}, \tag{2.5}$$

where z_i is the depth of the convective boundary layer. We take z_i as a constant, 600 m (Kahl, 1990; Serreze *et al.*, 1992; Bradley *et al.*, 1993; Tjernström and Graversen, 2009), because variability in it does not have much effect on our calculations.

We adopt the suggestion by Jordan *et al.* (1999) that a similar 'windless' coefficient is necessary for stable stratification but express it as

$$S_r = U_r + 0.5\mathrm{sech}(U_r). \tag{2.6}$$

Here, both U_r and S_r are in m s^{-1}. Equation (2.6) is similar to Mahrt's (2008) parametrization that includes a term to quantify mesoscale meandering flow where we have the sech term.

In effect, both (2.4) and (2.6) prevent a singularity in the bulk flux algorithm by making the transfer coefficients well behaved in light winds (cf. Godfrey and Beljaars, 1991; Fairall *et al.*, 1996; Zeng *et al.*, 1998; Andreas *et al.*, 2008). If we use U_r instead of S_r, the transfer coefficients must approach infinity to maintain finite fluxes as U_r approaches zero. But as U_r increases from zero, the S_r values calculated with either (2.4) or (2.6) quickly approach U_r for Arctic

conditions. For instance, when U_r reaches 2.2 ms^{-1}, S_r is already within 5% of U_r.

Because (2.1) and (2.2) are coupled through the Obukhov length (2.3), they must be solved iteratively using the mean measured or modelled conditions: namely, U_r, Θ_r, Q_r, and Θ_s. Moreover, (2.4) and our algorithms for z_T and z_Q also include u_*, as we will show. These equations must also be part of the iteration. That iteration usually converges in 3 to 5 steps.

In the analyses reported here, we found it more direct to estimate C_{DN10} than z_0 over summer sea ice (cf. Andreas *et al.*, 2010). These two parameters of momentum transfer are related through (2.2a), which in neutral stratification for a standard reference height of 10 m is

$$C_{\mathrm{DN10}} = \left\{ \frac{k}{\ln(10/z_0)} \right\}^2, \tag{2.7}$$

where z_0 must be in metres. The C_{DN10} values computed from (2.7) (once we first found z_0, as described later) are what we plotted in Figure 2.

Alternatively, the parametrization that we describe later predicts C_{DN10}. We obtain z_0 for use in (2.2) from this value by inverting (2.7).

3. The SHEBA data

The SHEBA ice camp drifted approximately 2700 km in the Beaufort Gyre between 2 October 1997 and 11 October 1998 (Uttal *et al.*, 2002). It started in the Beaufort Sea, drifted westward into the Chukchi Sea, then turned north into the Arctic Ocean near the date line.

During our SHEBA deployment, we had one central site in the SHEBA ice camp and, usually, four remote sites that ranged in distance from 0.25 to 30 km from the main camp. We serviced these remote sites about once a week either on foot, by snowmobile, or by helicopter, depending on ice conditions. Andreas *et al.* (1999, 2002, 2006, 2010), Persson *et al.* (2002), and Grachev *et al.* (2005, 2007a) describe the instruments that our Atmospheric Surface Flux Group (ASFG) deployed during SHEBA and review our data processing. Persson *et al.*, in particular, show pictures of the instruments at our main site.

The centrepiece of our site in the SHEBA camp was a 20 m tower instrumented at five levels with identical sonic anemometer/thermometers (K-type sonics from Applied Technologies, Inc.: ATI) and Vaisala HMP235 temperature and humidity sensors. The tower also held one Ophir fast-responding hygrometer that was mounted at 8 m, near the sonic at that level.

Through eddy-covariance measurements using standard turbulence processing, as described in Persson *et al.* (2002), Grachev *et al.* (2005, 2007a), and Andreas *et al.* (2006), we measured the momentum flux τ and the sensible heat flux H_s for each of the five tower levels and the latent heat flux H_L at one level (see (2.1)). This latter was the only direct, long-term measurement of latent heat flux from SHEBA.

The sonics also provided the mean wind speed in (2.1), U_r, at each level. The Vaisala HMP235s provided the mean temperature and specific humidity, Θ_r and Q_r, needed in (2.1).

Near this ASFG tower was a full suite of radiometers for measuring incoming and outgoing long-wave and short-wave radiation and several additional sensors for measuring surface temperature, Θ_s (e.g. Claffey *et al.*, 1999; Persson *et al.*, 2002). Here and for the remote sites, we processed the Eppley pyrgeometer data to obtain the long-wave radiative fluxes using the method that Fairall *et al.* (1998) recommend. That is, we measured both dome and case temperatures and corrected the fluxes with these.

Generally, for Θ_s we used the value implied by the emitted ($Q_{L\uparrow}$) and incoming ($Q_{L\downarrow}$) long-wave radiation measured by our pyrgeometers:

$$\Theta_s = (\sigma\,\varepsilon)^{-1/4}\{Q_{L\uparrow} - (1-\varepsilon)Q_{L\downarrow}\}^{1/4}. \tag{3.1}$$

Here, ε (= 0.99: Dozier and Warren, 1982; Warren, 1982; Jordan *et al.*, 1999) is the surface emissivity, and σ (= 5.67051×10^{-8} Wm^{-2}K^{-4}) is the Stefan–Boltzmann constant. See the SHEBA data archive at http://www.eol.ucar.edu/projects/sheba for tabulations and descriptions of these surface temperature data and the other datasets that we use in this study.

Our remote sites were instrumented with Flux-PAM (portable automated mesonet) stations from the National Center for Atmospheric Research instrument pool (Militzer *et al.*, 1995; Horst *et al.*, 1997). Our first four sites, which we deployed in October 1997, were named Atlanta, Baltimore, Cleveland, and Florida. The Cleveland station, however, was damaged by a pressure ridge in early February 1998 and removed from service for repairs.

The original Florida site was on smooth ice within 400 m of our main tower. Because of ice deformation, however, we extracted this PAM station and placed it and the refurbished Cleveland station next to our main tower for intercomparison during 1–20 April 1998. We then re-established the Florida site on a pressure ridge 250 m from our main tower, where it remained for the rest of the deployment.

In mid-April, we redeployed the refurbished Cleveland station at a new site called Seattle. Seattle, however, became untenable because of ice motions; and this PAM station was again redeployed in mid-June 1998 to a site named Maui. That Maui site lasted until late September 1998, as did the Atlanta, Baltimore, and Florida sites.

We have found the turbulence measurements from Seattle to be disturbed by a pressure ridge just upwind of the station and, thus, do not include data from that site in our analysis. We do use data from the other five PAM sites, however.

Each Flux-PAM station measured at one height the same quantities that we measured at the ASFG tower: wind speed and direction, temperature, relative humidity, and the turbulent fluxes of momentum and sensible heat. The website http://www.eol.ucar.edu/isf/projects/SHEBA contains instrument details, a history of each of the PAM sites deployed during SHEBA, and information on data processing.

Briefly, the PAM stations provided hourly averaged data, as did the main tower site. Each PAM station used a sonic anemometer/thermometer mounted at a height between 2.5 and 3.5 m, depending on instrument type, to measure the turbulent fluxes of momentum and sensible heat by eddy-covariance techniques (i.e. τ and H_s in (2.1)). We used sonics from both Gill (Solent R2) and Applied Technologies, Inc. (K-type), for the turbulence measurements at these sites.

Sonic anemometer/thermometers do not measure the instantaneous air temperature, $\widetilde{\theta}$ (= $\Theta + \theta$). Rather, the measured instantaneous 'sonic' temperature, $\widetilde{\theta}_s$, is a

combination of $\widetilde{\theta}$ and the instantaneous specific humidity, $\widetilde{q}$ $(= Q + q)$ (Schotanus *et al.*, 1983; Kaimal and Gaynor, 1991; Larsen *et al.*, 1993):

$$\widetilde{\theta}_s = \widetilde{\theta}(1 + 0.51\widetilde{q}). \tag{3.2}$$

This $\widetilde{\theta}_s$ is very close to the instantaneous virtual temperature,

$$\widetilde{\theta}_v = \widetilde{\theta}(1 + 0.61\widetilde{q}). \tag{3.3}$$

Consequently, the covariance between fluctuations in sonic temperature (θ_s) and in the vertical velocity (w) is

$$\overline{w\theta_s} = \overline{w\theta}(1 + 0.51Q) + 0.51\Theta\overline{wq}. \tag{3.4}$$

That is, this covariance is almost identical to the flux of virtual temperature required in the Obukhov length, (2.3), and can be used there directly with negligible error (e.g. Kaimal and Finnigan, 1994, p 224).

In some cases, though, obtaining the true sensible heat flux, $\rho\, c_p\overline{w\theta}$, from a sonic anemometer requires corrections based on (3.4) and an estimate of $\overline{wq}$. For the five sonics on our main tower, we made these small corrections using either the measured $\overline{wq}$ or a bulk flux estimate of $\overline{wq}$ (Persson *et al.*, 2002; Grachev *et al.*, 2005). The Flux-PAM stations, however, made no measurement of $\overline{wq}$; we consequently used $\overline{w\theta_s}$ directly to estimate $\overline{w\theta}$ for these. Because of the low humidity and small Bowen ratio over sea ice, $\overline{w\theta}$ and $\overline{w\theta_s}$ are typically within 5% of each other and are essentially interchangeable in our dataset (cf. Andreas *et al.*, 2005a; Grachev *et al.*, 2005).

To measure mean temperature and relative humidity at the Flux-PAM sites, we used Vaisala HMD50Y sensors in mechanically aspirated radiation shields (Andreas *et al.*, 2002). Each PAM station also measured barometric pressure with a Vaisala PTB 220B digital barometer. Because our main ASFG site had no measurement of barometric pressure, we used the pressure data from the Florida PAM site at the tower site also, because only a few hundred metres separated the two sites.

Each PAM station included sets of up-looking and down-looking radiometers to measure short-wave (Kipp and Zonen model CM21) and long-wave (Eppley model PIR) radiation. We obtained surface temperature at the PAM sites exclusively from these long-wave radiometers through (3.1).

We saw early in our SHEBA deployment that sensor riming was a problem at the PAM sites. Rime ice occasionally coated the domes of the radiometers (especially the up-looking ones) and, thereby, ruined the radiation measurements and our estimates of surface temperature. Rime also collected on the sonics; and when it coated the transducers, we lost wind information. In early March 1998, we installed effective heaters and blowers on all four radiometers at each site. This heating minimised the effects of dome icing for the rest of the experiment.

To mitigate riming on the PAM sonics, in mid-January 1998 we fixed heating tape around each transducer and at several locations along the support arms. The computer-controlled data acquisition system that monitored the PAM stations turned this heating on, however, only when it noticed that data returns from a sonic were deteriorating; and this heating remained on only until the data returns again reached 100%. We flagged these heating periods and did not use any flux data that were collected when the heaters were on.

The sonics and radiometers at our main site did not suffer as much from riming as the PAM instruments. First, someone was always attending the instruments at our main site and cleaning them as necessary. Second, the radiometers at our main site had effective blowers and heaters from the beginning of the experiment. Third, our 20 m tower was fitted exclusively with ATI sonics, which seemed to resist riming much better than the Gill sonics that were originally mounted on each PAM station. (We later replaced the Gill sonics with ATI sonics at the three most remote PAM sites.)

From the turbulent fluxes and mean meteorological quantities measured at multiple levels on our main tower and at the Flux-PAM sites, we could compute the turbulent transfer coefficients C_{Dr}, C_{Hr}, and C_{Er} from (2.1). These, in turn, give us estimates of the roughness lengths from (2.2):

$$z_0 = r\exp[-\{k\, C_{Dr}^{-1/2} + \psi_m(r/L)\}], \tag{3.5a}$$

$$z_T = r\exp[-\{k\, C_{Dr}^{1/2}C_{Hr}^{-1} + \psi_h(r/L)\}], \tag{3.5b}$$

$$z_Q = r\exp[-\{k\, C_{Dr}^{1/2}C_{Er}^{-1} + \psi_h(r/L)\}]. \tag{3.5c}$$

Here, the roughness lengths are in metres if r is in metres.

4. Uncertainty analysis and quality controls

Turbulence data generally have a lot of random scatter. Roughness lengths evaluated from these data, in turn, are commonly quite scattered because they derive from (3.5) and (2.1) and thus rely on several mean and turbulence variables. The only way to overcome this scatter is to collect a lot of high-quality data.

Table I summarises typical uncertainties in the quantities that we measured at the ASFG tower and at the PAM sites during SHEBA and in the variables that we calculate from these data. We base these estimates on previous similar summaries by Fairall *et al.* (1996) and Persson *et al.* (2002), on data analyses by Andreas *et al.* (2002), on similar uncertainty analyses by Andreas *et al.* (2005a, 2006), and on studies done for this paper. The main messages in Table I are that evaluations of z_0 are uncertain by a factor of 3, evaluations of z_T and z_Q are uncertain by a factor of 200, and C_{DN10} has an uncertainty of $\pm 11\%$.

In light of these uncertainties, we screened the data that we used in our analyses of z_0, z_T, z_Q, and C_{DN10} to ensure a reasonable signal-to-noise ratio. If any hour of data from a PAM station or from any level on the ASFG tower met the following criteria, we excluded the data as inadequate for determining z_0, z_T, z_Q, and C_{DN10}:

$$\tau \le 0\ \mathrm{N\,m^{-2}}, \tag{4.1a}$$

$$\left|H_s/\rho\, c_p\right| \le 0.005^{\circ}\mathrm{C\,m\,s^{-1}}, \tag{4.1b}$$

$$|H_L/\rho\, L_v| \le 2.5\times 10^{-7}(\mathrm{kg\,kg^{-1}})(\mathrm{m\,s^{-1}}), \tag{4.1c}$$

$$|\Theta_s - \Theta_r| \le 0.5^{\circ}\mathrm{C}, \tag{4.1d}$$

$$|Q_s - Q_r| \le 1.0\times 10^{-5}\mathrm{kg\,kg^{-1}}. \tag{4.1e}$$

Table I. Typical uncertainties in our hourly SHEBA measurements and in the variables that we calculate from these measurements

Variable	Uncertainty
Measured Variables	
Measurement height, r	± 0.3 m
Wind speed, U_r	± 0.03 m s^{-1}
Air temperature, Θ_r	± 0.2°C
Relative humidity, RH	$\pm 3\%$
Specific humidity, Q_r	$\pm 5\%$
Surface temperature, Θ_s	± 0.5°C
Surface specific humidity, Q_s	$\pm 5\%$
Friction velocity, u_*	± 0.02 m s^{-1}
Sensible heat flux, H_s	$\pm 20\%$
Latent heat flux, H_L	$\pm 20\%$
Calculated Variables	
Neutral-stability, 10 m drag coefficient, C_{DN10}	$\pm 11\%$
Roughness length for wind speed, z_0	$\frac{1}{3}$ – 3 times computed z_0
Roughness length for temperature, z_T	$\frac{1}{200}$ – 200 times computed z_T
Roughness length for humidity, z_Q	$\frac{1}{200}$ – 200 times computed z_Q

Only data that fail (4.1a) or (4.1b) prevent our computing z_0 and C_{DN10}. (Remember, we need H_s – actually $\rho\, c_p \overline{w\theta_s}$ – to compute the Obukhov length.) Data that fail (4.1a), (4.1b) or (4.1d) prevent our computing z_T. A failure to pass any of (4.1a), (4.1b), (4.1c) or (4.1e) prevent our computing z_Q.

As additional screening, if any calculated roughness lengths met the following criteria, we assumed the result was unrealistic and ignored it for our analyses of z_0, z_T, and z_Q:

$$z_0, z_T \text{ or } z_Q \geq 0.1 \text{ m}, \tag{4.2a}$$

$$z_T \text{ or } z_Q \leq 7 \times 10^{-8} \text{m}. \tag{4.2b}$$

We instituted (4.2a) because roughness lengths simply cannot be this large over sea ice (e.g. Banke *et al.*, 1980; Overland, 1985; Guest and Davidson, 1991; Andreas, 1995). The limit on z_0 in (4.2a) also implies that we did not let C_{DN10} be larger than 7.54×10^{-3}. The second limit, (4.2b), is the approximate mean free path of air molecules at sea level. We presume that the surface exchange of heat and moisture cannot occur at scales smaller than this (cf. Andreas and Emanuel, 2001; Andreas *et al.*, 2008).

In effect, the screening criteria (4.1) and (4.2) excluded from our analysis situations in which Monin–Obukhov similarity theory breaks down. In stable boundary layers, a host of phenomena occur that violate similarity theory: for example, the boundary layer may be so thin that a constant-flux layer does not exist, the turbulence may be only intermittent, gravity waves can confound the turbulence series, or a low-level jet rather than the surface may be the source of the turbulence (e.g. Mahrt, 1998, 1999; Grachev *et al.*, 2005). Tests (4.1) and (4.2) tended to keep us out of these regimes.

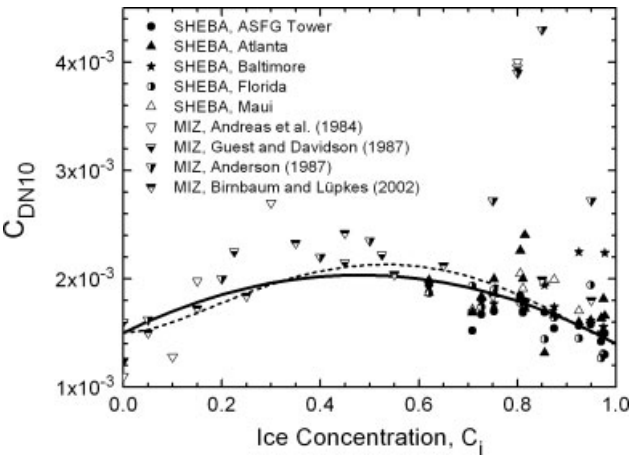

Figure 3. The 10-day averages of summer C_{DN10} values in Figure 2 from the ASFG tower and from the Flux-PAM sites called Atlanta, Baltimore, Florida, and Maui are plotted against ice concentration, C_i. The figure also shows C_{DN10} values obtained in the Antarctic marginal ice zone (MIZ; Andreas *et al.*, 1984) and the Arctic MIZ (Guest and Davidson, 1987; Anderson, 1987; Birnbaum and Lüpkes, 2002). The solid curve is (5.2); the dashed curve is Lüpkes and Birnbaum's (2005) Equation (22)

Because the five ASFG tower levels each had a sonic anemometer/thermometer and a temperature and humidity sensor, any hour of data could yield from none to five independent estimates of z_0 and z_T from this site. (We did use the same Θ_s for all estimates, though.) We do not report all of these values. Rather, we took the median value for all results that passed our screening for that hour. The median is the 'most common robust and resistant measure of central tendency' (Wilks, 2006, p 26). For example, later we will show plots of measured z_T/z_0 versus a bulk estimate of the roughness Reynolds number, $R_* = u_* z_0/\nu$. The plotted z_T and z_0 values will be the medians from all tower levels reporting z_T and z_0 for that hour. We also ran our bulk flux algorithm for all tower levels with sufficient data for it; the bulk u_* and z_0 are again the median values from all tower levels that yielded values. Hence, some of our hourly tower estimates are based on data from only one level, but some are based on data from all five levels.

Because of this 'averaging', we tend to have more confidence in the results from the ASFG tower than from the Flux-PAM stations, which did not have the luxury of redundant measurements. Taking the median value of the tower data also tends to mitigate the effects of fictitious correlation because, for example, the tower levels that yielded median measured values of z_T and z_0 did not always yield the median bulk estimates of u_* and z_0 that we used in comparing measured z_T/z_0 against bulk R_* in plots to follow.

5. Drag coefficient over summer sea ice and in the marginal ice zone

For the C_{DN10} data depicted in Figure 2, we assigned an ice concentration (defined as the fractional surface area of ice) appropriate for the middle of the averaging period. (Remember, the C_{DN10} markers represent 8, 10, or 11 days of averaged hourly data.) Figure 3 shows a plot of these averaged C_{DN10} values against ice concentration, C_i. We found C_i from the constraint

$$1 = C_i + C_L + C_P, \tag{5.1}$$

where C_L and C_P are, respectively, the area fractions of leads and melt ponds shown in Figure 2.

The SHEBA summer data, which are on the right side of Figure 3, for ice concentrations between 0.6 and 1.0, reiterate what we observed in Figure 2. As the ice concentration decreases or as the total water fraction ($C_w = 1 - C_i$) increases, C_{DN10} increases. An increasing water fraction means more vertical ice faces for the wind to push against and thereby to transfer momentum by form drag – that is, through pressure forces.

Classic studies in wind tunnels of momentum transfer over arrays of solid roughness elements (e.g. Marshall, 1971; Raupach *et al.*, 1980) and ensuing analyses (e.g. Wooding *et al.*, 1973; Arya, 1975; Raupach, 1992; MacDonald *et al.*, 1998; Shao and Yang, 2005) typically relate the effective roughness length or the drag coefficient over the array to the areal coverage of the obstacles. The data and analyses repeatedly show that, as the obstacle packing increases from sparse coverage to nearly complete coverage, the roughness length or the drag coefficient increases from a minimum, reaches a maximum for intermediate packing density, then decreases as the obstacles become more tightly packed.

The theoretical interpretation for these observations is as follows. With loose packing, all obstacles have high pressure on the upwind face and low pressure on the downwind face caused by flow separation. Thus, momentum transfer by pressure forces increases as the areal coverage of obstacles increases because of the increasing frontal area of the obstacles. As the obstacles become more tightly packed, however, the flow separation bubble downwind of an obstacle encroaches on the next obstacle. That obstacle is, thus, somewhat 'sheltered' by the upwind obstacle and does not feel the full force of the wind. As a result, momentum transfer becomes less efficient. Eventually, the packing becomes so tight that all vertical faces are sheltered, and transfer by pressure forces is ineffective. In short, z_0 and C_{DN10} are low for a surface with no obstacles, increase to maxima for intermediate packing density, then decrease to local minima for tightly packed obstacles.

Andreas *et al.* (1984) based their interpretation of C_{DN10} values measured in the Antarctic marginal ice zone (MIZ) on form drag arguments like these. Because marginal ice zones are mixes of ice and water, as is summer sea ice, we have added four sets of observations from marginal ice zones to Figure 3. The data from Andreas *et al.* (1984) are single-point observations for which C_{DN10} was based on radiosonde ascents. Guest and Davidson (1987) and Anderson (1987) obtained their data from inertial-dissipation measurements on ships in the East Greenland Sea. Generally, their data points represent multiple measurements for the given ice concentration. The data from Birnbaum and Lüpkes (2002) are a synthesis of multiple aircraft turbulence measurements collected during flights over the Fram Strait and reported by Hartmann *et al.* (1994) and Mai *et al.* (1996).

In Figure 3, all four sets of MIZ C_{DN10} values start at the open-ocean value, typically 1.5×10^{-3}, and increase from there with increasing ice concentration. Three of the MIZ sets include relatively large values for C_{DN10} for C_i on the order of 0.8, but the larger dataset from Birnbaum and Lüpkes (2002) reaches a maximum near $C_i = 0.6$ then falls right along the cluster of SHEBA values to the local minimum for compact sea ice.

Birnbaum and Lüpkes (2002) and Lüpkes and Birnbaum (2005) developed physically based parametrizations to describe the behaviour of the drag coefficient in the marginal ice zone. These models require knowing or parametrizing such physical quantities as the freeboard of the ice floes, the height of the ridge that generally borders floes in the MIZ, the width of typical floes, and the open water distance between floes. Through sensitivity studies, these models provide good insights into the processes and parameters that control momentum exchange in a sea ice environment that consists of both ice and water; but the models are much too complex for use in global climate models and even in sea ice models – they require too many unmeasured and unmodelled variables.

Lüpkes and Birnbaum (2005) realised the impracticality of their full model for large-scale computing and therefore simplified it to predict C_{DN10} as a function of just ice concentration. Following Andreas *et al.* (1984), we fitted by eye a second-order polynomial in ice concentration to the combined MIZ and SHEBA data in Figure 3 before we had seen the Lüpkes and Birnbaum paper. That fit is

$$10^3\, C_{DN10} = 1.500 + 2.233\, C_i - 2.333\, C_i^2, \qquad (5.2)$$

where C_i is still the fractional ice concentration ($0 \le C_i \le 1.0$). As do Lüpkes and Birnbaum, in fitting (5.2), we discounted the few large C_{DN10} values at large C_i from marginal ice zones: The 10 000 hours of SHEBA summer data at these concentrations overwhelm these outliers.

Figure 3 also shows the fit that Lüpkes and Birnbaum (2005) made to just their own MIZ data. This result is their Equation (22), which uses ice concentration as the only independent variable but requires specifying C_{DN10} over open water and over compact sea ice. We used 1.5×10^{-3} and 1.4×10^{-3}, respectively, for these values to obtain the Lüpkes and Birnbaum curve in Figure 3.

The Lüpkes and Birnbaum (2005) curve in Figure 3 is higher than third order in C_i and, therefore, more complex than our (5.2); but the two equations differ little in how well they represent the data shown in Figure 3. Because of its relative simplicity, we retain (5.2) in our bulk flux algorithm as the prediction for C_{DN10} (and, thus, z_0) for summer sea ice and in any marginal ice zone.

6. Estimating the turbulent heat fluxes

6.1. *Mosaic method*

In summer, when the Arctic surface is a patchwork of sea ice, melt ponds, and leads, estimating the sensible and latent heat fluxes, H_s and H_L, from a bulk flux algorithm might require weighted averages of the fluxes from the individual surfaces. With sensible heat flux as an example, this hypothesis is (cf. Andreas and Makshtas, 1985)

$$H_s = C_i\, H_{s,i} + C_L\, H_{s,L} + C_P\, H_{s,P}. \qquad (6.1)$$

Here, $H_{s,i}, H_{s,L}$, and $H_{s,P}$ are the fluxes that we would compute using (2.1b) over ice, leads, and melt ponds; and H_s is the area average. This approach is usually termed the mosaic method (e.g. Vihma, 1995).

On substituting (2.1b) for the various fluxes in (6.1), we obtain

$$\begin{aligned} H_s = {} & \rho_i\, c_{p,i}\, C_i\, C_{Hr,i}\, S_{r,i} \left(\Theta_{s,i} - \Theta_{r,i}\right) \\ & + \rho_L\, c_{p,L}\, C_L\, C_{Hr,L}\, S_{r,L} \left(\Theta_{s,L} - \Theta_{r,L}\right) \\ & + \rho_P\, c_{p,P}\, C_P\, C_{Hr,P}\, S_{r,P} \left(\Theta_{s,P} - \Theta_{r,P}\right). \end{aligned} \qquad (6.2)$$

Here, subscripts i, L, and P denote individual values appropriate over ice, leads, and melt ponds.

Because the leads and ponds were fairly small, we can assume that the air at reference height r was well mixed. Thus, we can approximate $S_{r,\mathrm{i}} = S_{r,\mathrm{L}} = S_{r,\mathrm{P}} = S_r$ and $\Theta_{r,\mathrm{i}} = \Theta_{r,\mathrm{L}} = \Theta_{r,\mathrm{P}} = \Theta_r$. Likewise, since the temperatures of the air and the various surfaces were all within a few degrees of 0°C in our SHEBA summer data (Andreas *et al.*, 2002; Persson *et al.*, 2002), we can further approximate $\rho_\mathrm{i} = \rho_\mathrm{L} = \rho_\mathrm{P} = \rho$ and $c_{p,\mathrm{i}} = c_{p,\mathrm{L}} = c_{p,\mathrm{P}} = c_p$. These conditions on wind speed and temperature further suggest that $C_{Hr,\mathrm{i}}$, $C_{Hr,\mathrm{L}}$, and $C_{Hr,\mathrm{P}}$ are all approximately equal. Call the common value C_{Hr}.

With these approximations, (6.2) simplifies to

$$H_\mathrm{s} = \rho\, c_p\, C_{Hr}\, S_r(\Theta_{s,\mathrm{Ave}} - \Theta_r), \tag{6.3}$$

where the areally averaged surface temperature is

$$\Theta_{s,\mathrm{Ave}} = C_\mathrm{i}\Theta_{s,\mathrm{i}} + C_\mathrm{L}\Theta_{s,\mathrm{L}} + C_\mathrm{P}\Theta_{s,\mathrm{P}}. \tag{6.4}$$

That is, over summer sea ice, when surface heterogeneities are small and air and surface are close to isothermal, we can approximate the areally averaged sensible heat flux with (2.1b) and a mosaic-based estimate of surface temperature. Incidentally, Overland *et al.* (2000) used equations comparable to (6.3) and (6.4) to estimate the regional sensible heat flux over *winter* Arctic sea ice.

Nearly the same sequence of equations and approximations that leads to (6.3) and (6.4) produces a similar conclusion for estimating the latent heat flux over summer sea ice. The only change is that we must account for the difference between the latent heat of sublimation over ice, L_s $(= L_\mathrm{v} + L_\mathrm{f})$, and the latent heat of vaporization, L_v, over the leads and ponds, where L_f is the latent heat of fusion. As a result, the equation analogous to (6.3) for the areally averaged latent heat flux has an extra term:

$$H_L = \rho\, L_\mathrm{s}\, C_{Er}\, S_r(Q_{s,\mathrm{Ave}} - Q_r)$$
$$-\rho\, L_\mathrm{f}\, C_{Er} S_r\{(Q_{s,\mathrm{Ave}} - Q_r) - C_\mathrm{i}(Q_{s,\mathrm{i}} - Q_r)\}. \tag{6.5}$$

Here, $Q_{s,\mathrm{Ave}}$ is obtained as is $\Theta_{s,\mathrm{Ave}}$ in (6.4) from specific humidities at the surfaces of the ice, leads, and ponds: $Q_{s,\mathrm{i}}$, $Q_{s,\mathrm{L}}$, and $Q_{s,\mathrm{P}}$, respectively. Moreover, in light of the scatter we find in H_L, we can ignore the second term on the right of (6.5) because it is at least eight times smaller than the first term (i.e. $L_\mathrm{s}/L_\mathrm{f} \approx 28.3/3.3$) and approaches zero as C_i approaches one.

With the conclusion above that C_{Hr} is uniform over summer sea ice, (3.5b) implies that the roughness length z_T is also uniform. In effect, both are now interpreted as area averages. We have hypothesised, though, that C_{Hr} for use in (3.5b) to find z_T must be obtained from (6.3) and our measured value of H_s.

During the SHEBA summer, T. C. Grenfell (2003, personal communication) made sporadic measurements of the surface temperatures of leads and melt ponds in the vicinity of the SHEBA camp. From these data, from the values of C_i, C_L, and C_P that we used to make Figures 2 and 3, and from our own measurements of $\Theta_{s,\mathrm{i}}$ near the ASFG tower, we created a rudimentary time series of $\Theta_{s,\mathrm{Ave}}$ for summer. We say 'rudimentary' here because we had only occasional values of $\Theta_{s,\mathrm{L}}$, $\Theta_{s,\mathrm{P}}$, C_L, and C_P (once a week, on average). We interpolated those to be compatible with our hourly measurements of $\Theta_{s,\mathrm{i}}$.

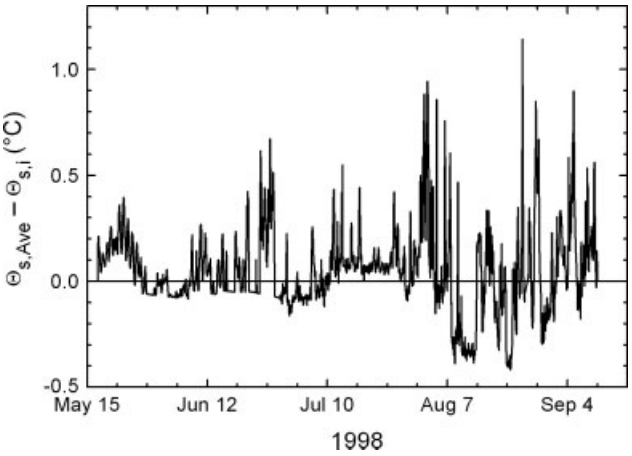

Figure 4. Time series for summer of the difference between the average surface temperature calculated from (6.4), $\Theta_{s,\mathrm{Ave}}$, and hourly measurements of the ice surface temperature, $\Theta_{s,\mathrm{i}}$, obtained through (3.1) from measurements near the Atmospheric Surface Flux Group tower in the SHEBA camp

Andreas *et al.* (2005b) reported evaluating z_T using this average surface temperature in combination with flux data from the ASFG tower. For comparison, they also evaluated z_T from this same data but with just $\Theta_{s,\mathrm{i}}$ as the surface temperature. The two sets of z_T values were negligibly different.

Figure 4 explains this null result. It shows the difference between $\Theta_{s,\mathrm{Ave}}$ and $\Theta_{s,\mathrm{i}}$ for summer. This difference is biased slightly positive: Its average from Figure 4, 0.05°C, is statistically different from zero but not practically different from zero. And rarely is the absolute value of this difference larger than 0.5°C. Remember (4.1d): We do not have much confidence in estimates of C_{Hr} when the surface–air temperature difference has an absolute value of 0.5°C or less. Similarly, we cannot expect much signal-to-noise ratio in estimates of C_{Hr} (and z_T) when we apply the mosaic method but the areally averaged surface temperature ($\Theta_{s,\mathrm{Ave}}$) is within 0.5°C of the temperature of the main surface component – the sea ice ($\Theta_{s,\mathrm{i}}$).

The long-wave radiation budget may be the physical explanation for this seeming uniformity in surface temperature. During SHEBA summer, the average cloud fraction was above 80% (Intrieri *et al.*, 2002). As a result, the net flux of long-wave radiation was, on average, slightly upward but within 20 Wm^{-2} of zero (Intrieri *et al.*, 2002). That is, the clouds and the surface were near radiative equilibrium – a condition that would tend to homogenise surface temperatures.

In conclusion, although the mosaic method is the formally more accurate way to evaluate heat fluxes over heterogeneous surfaces, summer sea ice does not seem to be thermally heterogeneous enough to make the method practically important. Henceforth, the values of z_T and z_Q that we report were obtained with $\Theta_{s,\mathrm{i}}$ as the surface temperature in (2.1b) and with Q_s in (2.1c) evaluated as the saturation specific humidity at $\Theta_{s,\mathrm{i}}$.

On the other hand, for marginal ice zones, especially in seasons other than summer, when ice and ocean will have much different surface temperatures, using the mosaic technique will likely be essential for estimating areally averaged sensible and latent heat fluxes (e.g. Andreas and Makshtas, 1985).

6.2. *Finding the scalar roughness lengths*

The scalar roughness length z_s, where z_s is either z_T or z_Q (see (2.2)), is usually expressed as the ratio z_s/z_0. Many sources corroborate that z_s/z_0 should depend on the roughness Reynolds number, $R_* = u_* z_0/\nu$, where ν is the kinematic viscosity of air (e.g. Garratt and Hicks, 1973; Liu *et al.*, 1979; Brutsaert, 1982, p 89 ff.).

Our candidate expression for the scalar roughness is Andreas's (1987) theoretical model:

$$\ln(z_s/z_0) = b_0 + b_1 \ln R_* + b_2 (\ln R_*)^2. \qquad (6.6)$$

Andreas (1987, 2002) tabulates the polynomial coefficients b_0, b_1, and b_2, which are different sets for z_T and z_Q. Briefly, according to this model, z_Q is 13–40% larger than z_T – primarily because the molecular diffusivity of water vapour in air is larger than the molecular diffusivity of heat in air.

For the five SHEBA summer flux sites, we used (3.5b) and (3.5c) to obtain estimates of z_T and z_Q for all the hourly data that passed the quality controls described in section 4. Figure 5 shows z_T/z_0 as a function of roughness Reynolds number for all the surviving summer data. Table II shows that this figure summarises over 1100 hours of data.

Figure 6 shows a comparable plot of z_Q/z_0 versus the roughness Reynolds number. Because our only measurements of the latent heat flux were at one level on the Atmospheric Surface Flux Group tower, Figure 6 shows fewer points than in Figure 5 (see Table II).

One hazard in plotting z_T/z_0 and z_Q/z_0 versus R_* to test (6.6), however, is fictitious correlation. $R_* = u_* z_0/\nu$, z_T/z_0, and z_Q/z_0 all obviously include z_0; and u_* appears in the evaluations of z_0, z_T, and z_Q. Andreas (2002) demonstrated that, as a result of these shared variables, plots of z_T/z_0 and z_Q/z_0 versus R_*, where all quantities are measured, suffer from fictitious correlation such that the plotted data tend to follow the slope that (6.6) predicts.

If we use our bulk flux algorithm to compute R_*, however, the same measured u_* and z_0 do not appear in both dependent and independent variables, and the fictitious correlation is mitigated. Andreas *et al.* (2006) first suggested using a bulk estimate of R_* to parametrize another set of turbulence measurements (see also Andreas *et al.* (2010)). We denote this bulk estimate as $R_{*,\mathrm{B}} = u_{*,\mathrm{B}} z_{0,\mathrm{B}}/\nu$, where $u_{*,\mathrm{B}}$ and $z_{0,\mathrm{B}}$ come from our bulk flux algorithm.

Moreover, the objective of a bulk flux algorithm is to predict accurate values of z_T/z_0 and z_Q/z_0 from the algorithm's estimate of R_*. Consequently, comparing measured values of z_T/z_0 and z_Q/z_0 with the bulk estimate of R_*, $R_{*,\mathrm{B}}$, as we do in Figures 5 and 6, is the proper way to test or develop a parametrization for the scalar roughness length.

The clouds of hourly data in Figures 5 and 6 are scattered, but this spread is not surprising in light of the uncertainties in z_0, z_T, and z_Q that we summarised in Table I. A lot of high-quality data are therefore required to obtain meaningful estimates of the average behaviours of z_T/z_0 and z_Q/z_0. The black circles in Figures 5 and 6 are therefore bin averages of the hourly data such that there are four evenly spaced $R_{*,\mathrm{B}}$ bins per decade.

These bin averages are computed as geometric means rather than arithmetic means. Measured roughness lengths have distributions that are approximately log-normal (Vickers and Mahrt, 2006). The geometric mean, which is based on the average of the logarithms of the values within a bin, is a better indicator of the central tendency of the distribution than is the arithmetic mean, which is biased high by the largest values in the bin. The error bars on these bin averages are likewise computed as two standard deviations in the bin mean, where the standard deviation is also calculated from the logarithms of the hourly values in the bin.

These bin averages in Figures 5 and 6 corroborate Andreas's (1987) model. In each figure, four of the five averages in the highest $R_{*,\mathrm{B}}$ bins are within two standard deviations of the model. That is, these averages validate the model's predictions for the magnitudes of z_T/z_0 and z_Q/z_0 and its prediction that both z_T/z_0 and z_Q/z_0 decrease with increasing roughness Reynolds number.

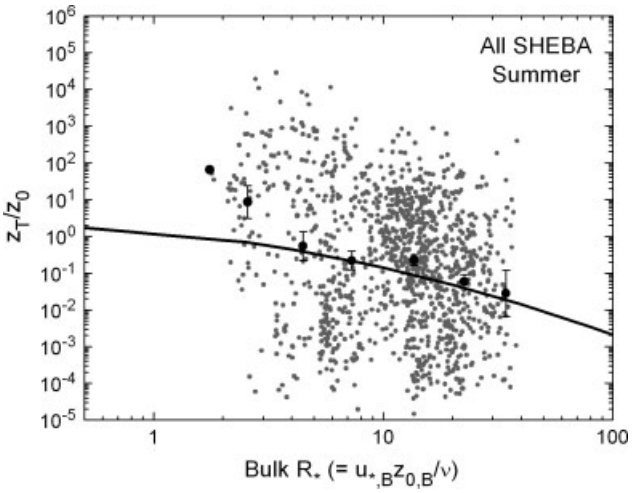

Figure 5. Hourly measurements of z_T/z_0 (grey circles) for summer from the ASFG tower and the Flux-PAM sites called Atlanta, Baltimore, Florida, and Maui are plotted against estimates of the roughness Reynolds number from our bulk flux algorithm. The black circles are bin averages, and the error bars represent ±2 standard deviations in these bin averages. The curve is Andreas's (1987) model, (6.6). This figure summarises 1177 hours of data (see Table II)

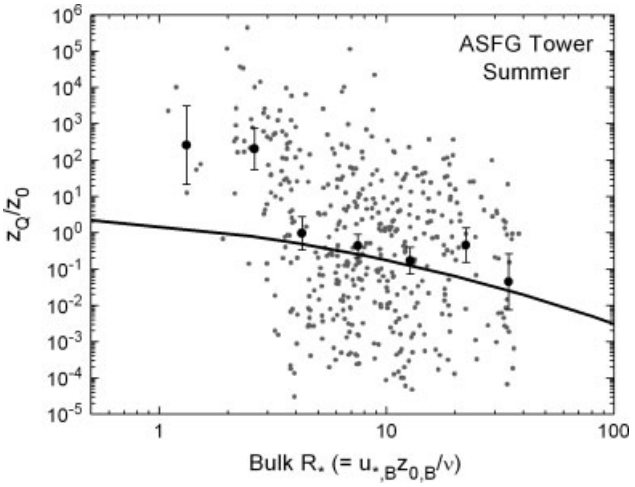

Figure 6. Hourly measurements of z_Q/z_0 (grey circles) for summer from the 8 m level on the Atmospheric Surface Flux Group tower are plotted against the roughness Reynolds number from our bulk flux algorithm. The black circles are bin averages, and the error bars represent ±2 standard deviations in these bin averages. The curve is Andreas's (1987) model, (6.6). This figure summarises 439 hours of data (see Table II)

Table II. Hours of summertime data from various SHEBA sites that were used in analyses and figures presented in this paper

Figures	C_{DN10} 2, 3 (h)	z_T/z_0 5 (h)	z_Q/z_0 6 (h)	u_* 7, 10 (h)	H_s 8, 11 (h)	H_L 9 (h)
Site						
ASFG Tower	2071	290	439	1943	2044	1697
Atlanta	2065	192		2237	2305	
Baltimore	2346	200		2650	2699	
Cleveland (only winter)	268					
Florida	1911	261		2570	2666	
Maui	2111	234		1889	1925	

At small $R_{*,B}$, two averages in each plot are above the model curve; but these bins contain fewer hourly values as evidenced by the generally larger error bars. In fact, the left-most black circle in Figure 5 has no error bars because that bin 'average' consist of only one hourly z_T/z_0 value.

Although the model (6.6) has seen relatively wide use in studies of turbulent exchange over ice and snow (e.g. Launiainen and Vihma, 1990; Jordan *et al.*, 1999; Andreas *et al.*, 2004; Reijmer *et al.*, 2004), it has not been fully validated over sea ice. Andreas (2002) tested (6.6) with data from the literature, but these data were collected over snow-covered ground and glaciers. Likewise, Smeets *et al.* (1998) and Denby and Snellen (2002) tested the z_T prediction from (6.6) with data collected over Austrian and Icelandic glaciers, respectively, and found good agreement. In another glacier study using data from Greenland and Iceland, Smeets and Van den Broeke (2008) found (6.6) to represent their z_T and z_Q data well for $5 < R_* < 60$ but not as well for larger roughness Reynolds numbers.

Evidently, only Andreas *et al.* (2005a, 2010) and Brunke *et al.* (2006) have tested (6.6) with flux data collected over sea ice. Andreas *et al.* (2005a) used winter data from Ice Station Weddell, and Brunke *et al.* used these same SHEBA data. Andreas *et al.* (2010) reanalysed the SHEBA winter data; our work here is the complementary summer analysis and the first to focus exclusively on summer sea ice. We felt it was necessary to repeat some of the work in Brunke *et al.* for two reasons: They did not study the behaviour of z_Q; and we have introduced new techniques to mitigate the effects of fictitious correlation.

With Figures 5 and 6, we confirm that (6.6) is a good parametrization for z_T and z_Q for $R_{*,B}$ values between 1 and 40, the largest roughness Reynolds number represented in our summer dataset. We therefore retain (6.6) as the parametrization for z_T and z_Q in our bulk flux algorithm.

7. Flux comparisons

Let us now look at how the bulk flux algorithm that we have described performs in representing the measured turbulent fluxes. We again use the SHEBA summer data for these comparisons, but our approach is not based on circular logic. That is, we are not testing our algorithm with only the same data that we have used to develop it. First, our polynomial parametrization for C_{DN10}, shown in (5.2) and Figure 3, relies on data collected in marginal ice zones as well as on the summer SHEBA data. Furthermore, that fit was made by eye rather than statistically. In other words, the fit was not made by formally minimising statistical errors in the data. Finally, Table II shows that slightly different data were used to obtain the C_{DN10} values in Figure 3 and the u_* values that we show soon in Figure 7.

Similarly, our upcoming plots that compare measured and modelled sensible and latent heat fluxes do not suffer from circular logic either. The key to predicting the fluxes is good predictions for z_T and z_Q. Although Figure 5 and 6 confirm that, on average, the SHEBA summer data agree well with Andreas's (1987) model predictions for z_T/z_0 and z_Q/z_0, (6.6), we have not used those data in any way to tune that model. In our bulk flux algorithm, we use (6.6) exactly as it was published in 1987. Secondly, Table II summarises the number of hours of data depicted in Figures 5 and 6 and in our plots of sensible and latent heat fluxes to follow, Figures 8 and 9, respectively. We use many more hours of data in our plots that compare fluxes than in the plots that validate our predictions for z_T/z_0 and z_Q/z_0, Figures 5 and 6, because we now ignore the screening conditions (4.1) and (4.2) and use all available data.

Figure 7 compares measured and modelled values of the friction velocity for the five SHEBA summer sites. From Table II, we see that these plots represent over 11 000 hours of data.

To evaluate the performance of our flux algorithm, we computed two metrics, following Willmott (1982). Let M_i be a measured flux (i.e. u_*, H_s, or H_L) and let B_i be the corresponding estimate of that flux from our bulk flux algorithm. The mean bias error in the modelled (bulk) values is

$$\mathrm{MBE} = \frac{1}{N}\sum_{i=1}^{N}(B_i - M_i), \tag{7.1}$$

where N is the number of observations (see Table II). The root-mean-square error in the modelled values is

$$\mathrm{RMSE} = \left\{\frac{1}{N}\sum_{i=1}^{N}(B_i - M_i)^2\right\}^{1/2}. \tag{7.2}$$

Table III list these metrics for the comparisons shown in Figure 7.

In each panel in Figure 7, the best fitting line through the data is very close to the 1:1 line. The metrics in Table III reiterate how well our bulk flux algorithm does in predicting

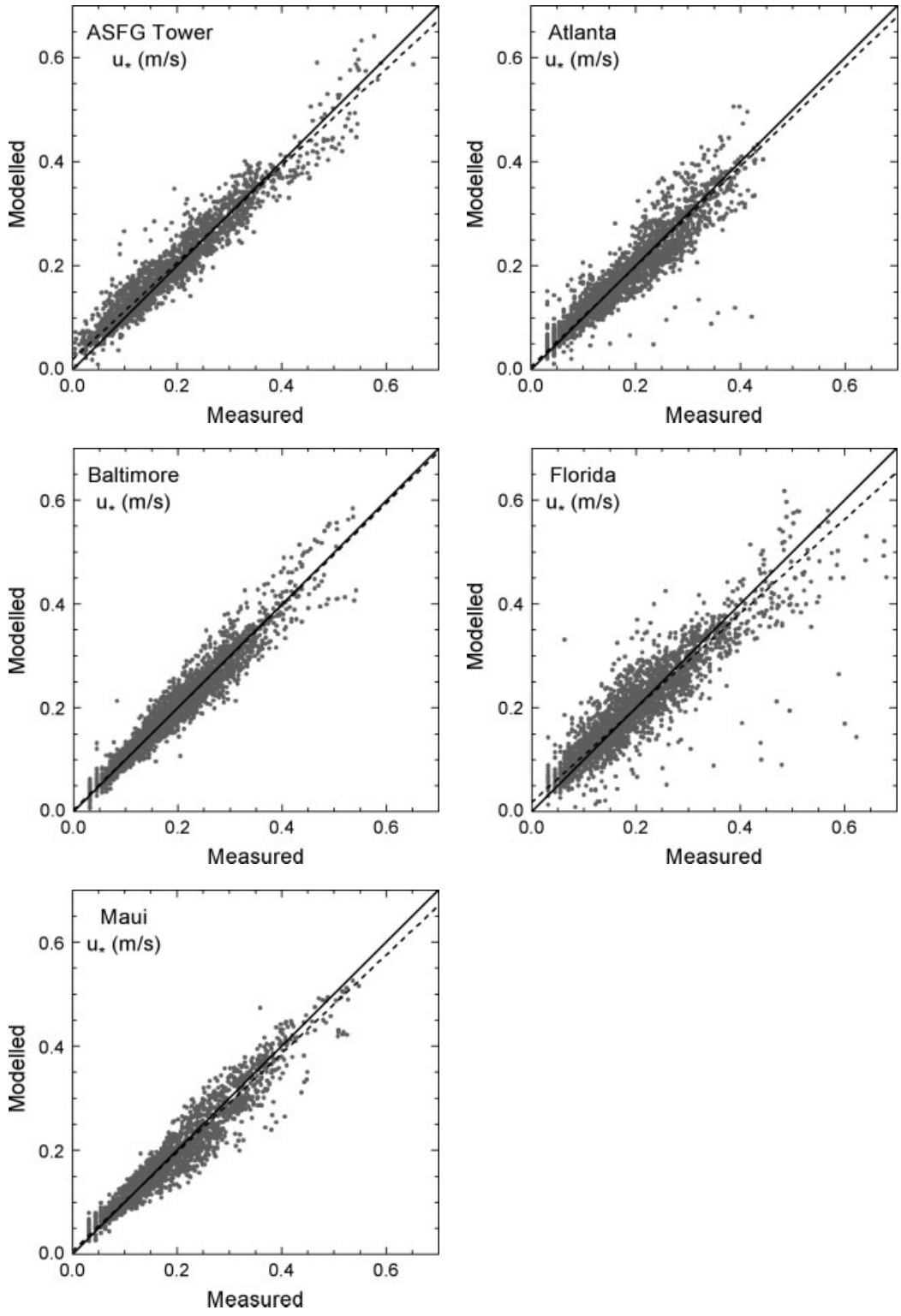

Figure 7. Scatter plots of the friction velocity, u_*, measured on the Atmospheric Surface Flux Group tower and at the Flux-PAM sites named Atlanta, Baltimore, Florida, and Maui during summer and modelled with our bulk flux algorithm using data from those sites. In each panel, the solid line is 1:1. The dashed line is the best fit through the data, taken as the bisector of y-versus-x and x-versus-y least-squares fits (e.g. Andreas, 2002). Table II lists the hours of data in each plot; Table III summarises the model metrics

u_* over summer Arctic sea ice. The absolute value of the bias error in all five examples is well less than 0.01 m s^{-1}, and the sign is both positive and negative. The root-mean-square error, which is a measure of the scatter in the data, is typically 0.03 m s^{-1}. Under the reasonable assumption that approximately half of the mean-square error is attributable to measurement uncertainty and half to model uncertainty, we can assess the absolute accuracy of our bulk flux algorithm for estimating u_* as RMSE/$\sqrt{2}$, which is 0.02–0.03 m s^{-1}.

Figure 8 compares measured and modelled values of the sensible heat flux, H_s, for all five of the SHEBA summer sites. These plots likewise represent over 11 000 hours of data (see Table II). As usual, obtaining any modelled flux (in this case, H_s) requires iterating on the full set of equations

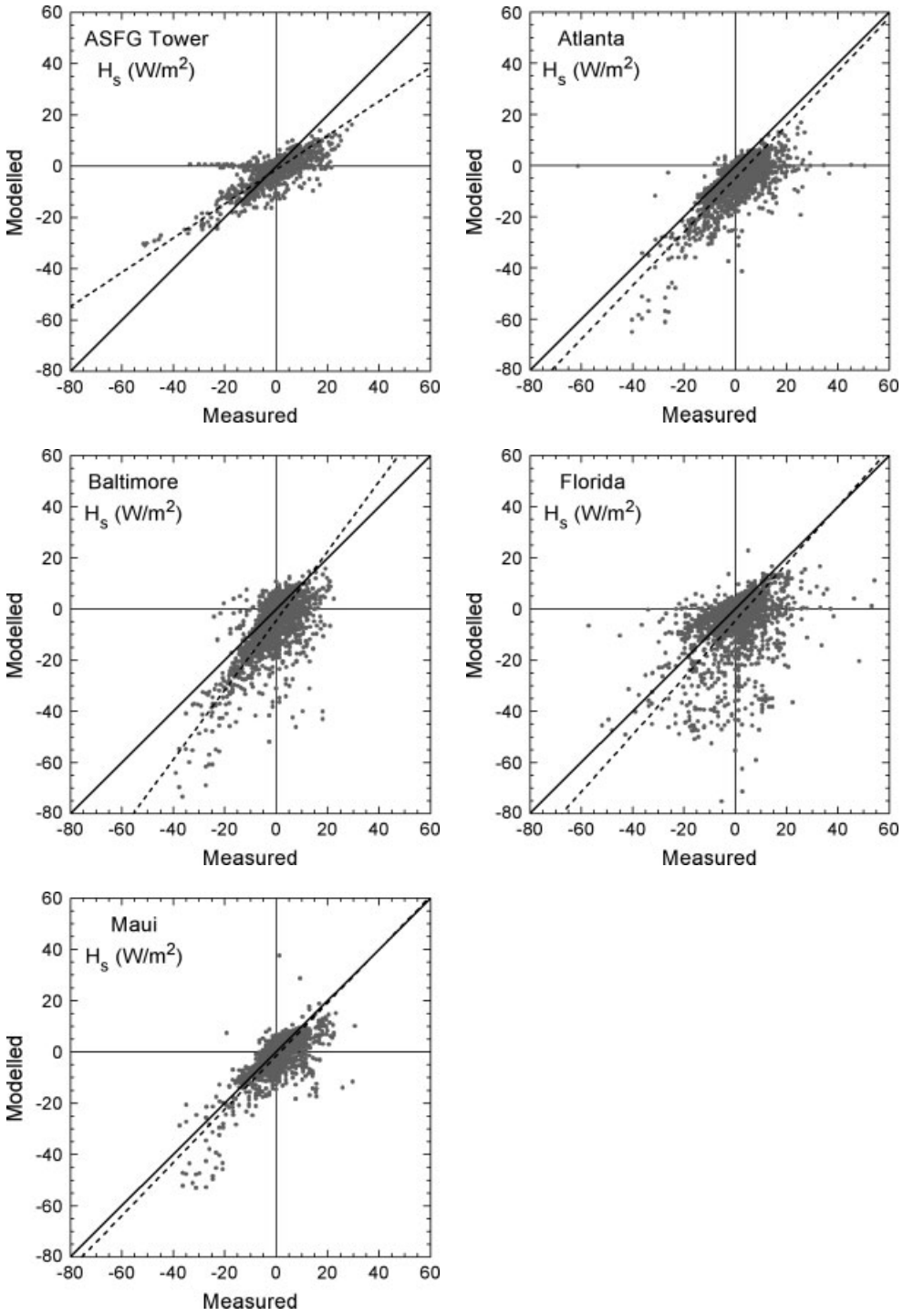

Figure 8. As in Figure 7, except the panels compare measured and modelled values of the sensible heat flux, H_s

that constitute our bulk flux algorithm: (2.1)–(2.7), (5.2) and (6.6). In these and in our later heat flux plots, Figures 9 and 11, a positive flux is upward – from surface to air (see (2.1b) and (2.1c)).

The results in Figure 8 are somewhat mixed. The ASFG tower and Maui panels have the smallest mean bias errors and root-mean-square errors among the five panels (Table III). But while the Maui results trend fairly well toward the 1:1 line, the ASFG tower points deviate from 1:1 because of some measured fluxes with large absolute values.

In general, though, the range of measured and modelled fluxes – typically between −20 and +20 W m^{-2} – emphasises the difficulties in both measuring and modelling sensible heat flux over summer sea ice. The vertical temperature gradients are small, and the magnitudes of the fluxes are small; errors in either quantity thus severely degrade comparisons between measured and modelled fluxes. Nevertheless, atmospheric models must still estimate the sensible heat flux over summer sea ice. The panels in Figure 8 demonstrate how accurate these model estimates might be.

Table III lists the fitting metrics for all the sites shown in Figure 8. For the five sites, the mean bias error ranges from −1.4 to −5.0 W m^{-2}. That is, the bias error is always negative; at least for the SHEBA dataset, our bulk flux algorithm is biased low in its predictions of sensible heat flux over summer sea ice.

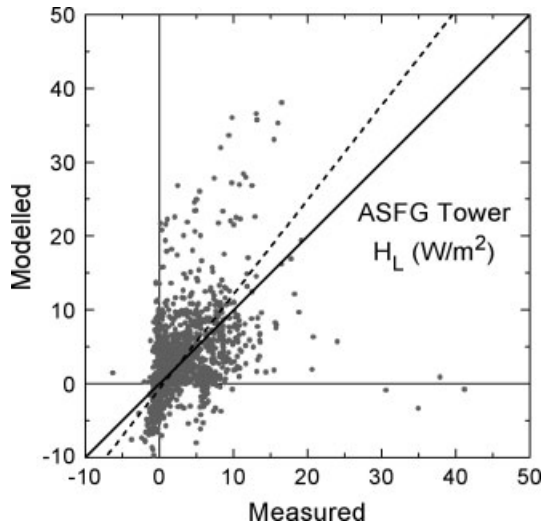

Figure 9. As in Figure 7, except this plot shows the one comparison between measured and modelled latent heat flux that is possible in the SHEBA dataset – from measurements made on the Atmospheric Surface Flux Group tower

The root-mean-square errors (RMSE) for the five panels in Figure 8 range from 5.5 to 11.3 W m^{-2}. Again, under the assumption that half of the mean-square error is attributable to the measurements and half to the algorithm, we use RMSE/$\sqrt{2}$, which is typically 6 W m^{-2}, as an estimate of the general precision in our algorithm's prediction for sensible heat flux in the summer.

Figure 9 shows the only comparison between measured and modelled latent heat flux possible with our SHEBA dataset – values based on data from the Atmospheric Surface Flux Group tower. Again, the range of fluxes in this plot – typically from 0 to 10 W m^{-2} – implies how difficult measuring and modelling latent heat flux is over sea ice.

The best fit through the data in Figure 9 deviates a bit from the 1:1 line – primarily because of some seemingly unrealistically large modelled fluxes that do not correspond with comparable measured values. The fitting metrics in Table III, however, suggest that our algorithm does better in estimating the latent heat flux than the sensible heat flux. The mean bias error in latent heat flux is only 0.05 W m^{-2}. The root-mean-square error in the latent heat flux plot, 5.0 W m^{-2}, is also smaller than any of the comparable errors in the sensible heat flux plots for the five SHEBA summer sites.

As above, we assign half of the mean-square error to uncertainty in our flux algorithm. Thus, an estimate of the absolute accuracy of our bulk flux algorithm's ability to estimate latent heat flux is RMSE/$\sqrt{2}$, which is 3.5 W m^{-2}.

8. An alternative algorithm

As a demonstration of the improved predictions our new algorithm offers, we compare it with the Community Ice Code (CICE; Hunke and Lipscomb, 2008). The CICE module is an integral part of the Community Climate System Model (Briegleb *et al.*, 2004) and, as such, is a crucial tool for climate studies (e.g. Kiehl and Gent, 2004; Collins *et al.*, 2006; Holland *et al.*, 2006). Although CICE is much more than a bulk turbulent flux algorithm, surface flux calculations are essential in it; and it parametrizes these fluxes using the same formalism that our algorithm does. Because CICE differs in detail from our algorithm, however, it is a worthy alternative for testing the efficacy of the presumed improvements in our algorithm.

CICE assumes $z_0 = z_T = z_Q = 5.0 \times 10^{-4}$ m. Although it uses the Paulson (1970) functions for ψ_m and ψ_h in unstable stratification, as does our algorithm, it uses the functions from Holtslag and De Bruin (1988) in stable stratification. Remember, our new algorithm uses the functions from Grachev *et al.* (2007a). Finally, CICE does not have a gustiness parametrization, like our (2.4), in unstable stratification but does parametrize windless transfer in stable stratification – for the sensible heat flux only – following Jordan *et al.* (1999) (cf. our (2.6)). In effect, for stable stratification, CICE adds to all computed sensible heat fluxes 1Wm^{-2} K^{-1} $(\Theta_s - \Theta_r)$. Consequently, all negative fluxes become more negative.

Figures 10 and 11 compare u_* and H_s values measured at the Flux-PAM sites Atlanta and Baltimore with values modelled with the surface flux algorithm in CICE. Compare these plots with similar plots in Figures 7 and 8 for which the modelled values come from our new algorithm. We chose Atlanta and Baltimore for these comparisons because they have long records of summer data but, unlike the

Table III. Performance of the SHEBA bulk flux algorithm depicted in Figures 7–9 and the Community Ice Code (CICE) algorithm depicted in Figures 10 and 11

Site	u_* (m s^{-1})		H_s (W m^{-2})		H_L (W m^{-2})	
	MBE	RMSE	MBE	RMSE	MBE	RMSE
SHEBA Algorithm						
ASFG Tower	0.0062	0.0300	−1.4	5.5	0.05	5.0
Atlanta	−0.0008	0.0339	−5.0	8.2		
Baltimore	0.0004	0.0233	−4.8	8.7		
Florida	−0.0004	0.0453	−4.5	11.3		
Maui	−0.0038	0.0285	−1.6	5.7		
CICE Algorithm						
Atlanta	−0.0059	0.0318	−6.6	10.6		
Baltimore	−0.0054	0.0236	−6.6	12.0		

The mean bias error (MBE) and the root-mean-square error (RMSE) are computed according to (7.1) and (7.2). Table II gives the number of observations used in each set of calculations.

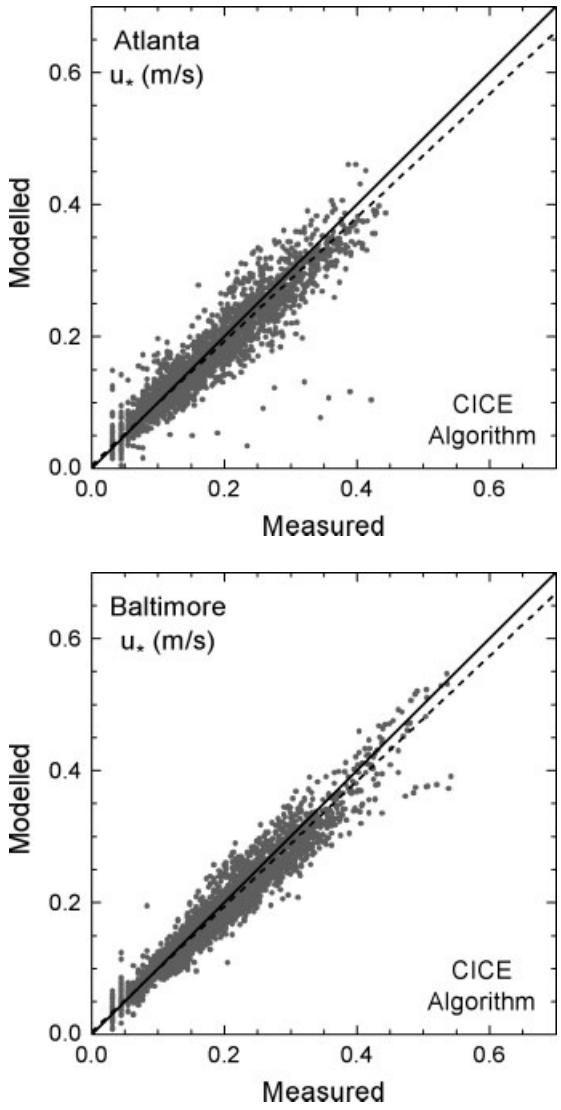

Figure 10. As in Figure 7, except this shows only the Flux-PAM sites Atlanta and Baltimore; and the bulk flux algorithm used to compute the modelled flux comes from the Community Ice Code, CICE. Table II again lists the hours of data in each panel; Table III summarises the model metrics

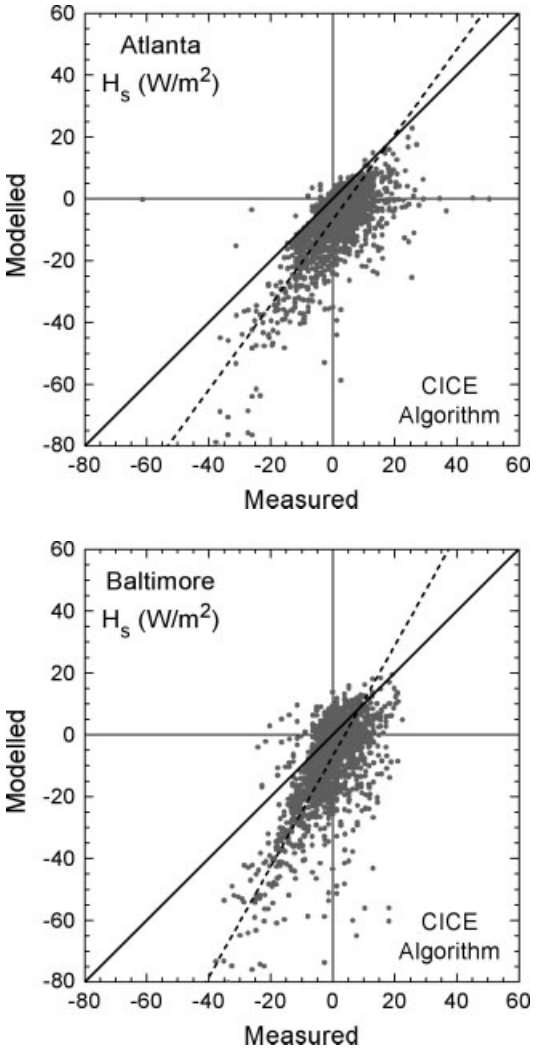

Figure 11. As in Figure 10, except the panels compare measured and modelled values of the sensible heat flux, H_s

ASFG tower, have only one measurement height. They thus provide a data source similar to what a regional or climate model would be replicating.

In Figure 10, u_* values modelled with the CICE algorithm are biased low for both PAM stations. On the other hand, the Atlanta and Baltimore panels in Figure 7 show virtually no model bias in u_*. Table III confirms these visual results; the mean bias errors in the CICE prediction of u_* are significantly more negative than for our new SHEBA algorithm. The scatter in the two panels in Figure 10 – as quantified by the root-mean-square error in Table III – is not very different from the scatter in Figure 7.

We attribute the negative mean bias errors in Figure 10 to the constant value of z_0, 5.0×10^{-4} m, in the CICE algorithm. This z_0 value corresponds to a C_{DN10} value of 1.63×10^{-3}. Figure 3 shows that, although summer C_{DN10} values can occasionally be smaller than 1.63×10^{-3}, they are more often considerably larger. The CICE algorithm simply always underestimates C_{DN10} during the height of summer.

Figure 11 presents similar comparisons of H_s measured at Atlanta and Baltimore and modelled with the CICE algorithm. The agreement between measured and modelled sensible heat flux is noticeably poorer than for the comparable panels in Figure 8, where the modelled H_s is based on our new algorithm. The values for mean bias error (MBE) and root-mean-square error in Table III reiterate the poorer performance of the CICE algorithm; the MBEs are significantly more negative for both PAM sites in Figure 11, and the RMSE values are both at least 25% larger than for fluxes modelled with our new algorithm.

Furthermore, both panels in Figure 11 show that the CICE algorithm overestimates the magnitude of H_s (compared to the Atlanta and Baltimore panels in Figure 8) when H_s is negative. As a result, both fitting lines in Figure 11 are rotated significantly counter-clockwise from the 1:1 line. With (2.6) and the new stratification corrections from Grachev *et al.* (2007a), we have focused our developmental efforts on improving flux parametrizations in stable stratification. When compared with Figure 8, the results in Figure 11 confirm that these were beneficial improvements.

9. Conclusions

Using the longest set of turbulent flux data ever collected over sea ice – data from SHEBA – we have developed and tested parametrizations for the turbulent fluxes of momentum and

sensible and latent heat over summer sea ice. Ours is an aerodynamic definition of summer as the period when the ocean surface is a mosaic of sea ice and water in both leads and melt ponds. In the SHEBA dataset at the height of summer, water covered about 40% of the surface.

The leads and melt ponds of summer produce vertical ice faces that the wind can push against; momentum transfer to the surface is thereby enhanced by form drag. And this enhanced momentum exchange seems to homogenise the atmospheric surface layer despite the visual heterogeneity of the surface. As an example, Figure 2 shows that, among the several SHEBA sites, the neutral-stability drag coefficient at a reference height of 10 m, C_{DN10}, behaves more coherently in summer than in winter.

Because marginal ice zones are other ocean regions where the surface consists of ice and open water, we have merged our SHEBA measurements of C_{DN10} with comparable measurements made in marginal ice zones. These various datasets yield a consistent picture of how C_{DN10} varies with ice concentration. The drag formulation in our bulk flux algorithm, (5.2), therefore simply predicts C_{DN10} over summer sea ice and in any marginal ice zone from a second-order polynomial in ice concentration, C_i. Because $C_i = 1 - C_w$, where C_w is the fractional surface area of water, to employ our algorithm, sea-ice models must include a parametrization for melt pond coverage because the area of these is included in C_w.

Other essential components of our bulk turbulent flux algorithm are predictions for the roughness lengths for temperature (z_T) and humidity (z_Q). The sensible heat flux data from five SHEBA sites support Andreas's (1987) model for predicting z_T/z_0, (6.6). Results from the lone long-term latent heat flux measurement site during SHEBA – at one level on the Atmospheric Surface Flux Group tower – also support Andreas's predictions for z_Q/z_0.

Because z_T/z_0 and z_Q/z_0 are theoretically related to the roughness Reynolds number, $R_* = u_* z_0/\nu$, plots to study this relationship must be made carefully to minimise the fictitious correlation that results because of the shared variables z_0 and u_*. When z_T/z_0, z_Q/z_0 and R_* are all calculated from measured values, the fictitious correlation can be severe and, thus, misleading. We have here introduced a method to mitigate the fictitious correlation by forming z_T/z_0 and z_Q/z_0 from data but computing R_* from our bulk flux algorithm. In fact, this is the way that parametrizations for roughness lengths should be developed and tested: The goal of a bulk flux algorithm is to predict accurate values of z_T and z_Q from the algorithm's estimate of R_*.

Other components of our bulk flux algorithm are equations (2.1)–(2.7) and expressions for the stability corrections in (2.2), ψ_m and ψ_h. From the SHEBA data, Grachev *et al.* (2007a) developed new expressions for ψ_m and ψ_h in stable stratification that we incorporated into our algorithm.

Based on the error analyses associated with our flux comparisons in Figures 7–9, we believe that our flux algorithm can estimate u_* over summer sea ice to 0.02–0.03 m s^{-1} and with negligible bias for u_* values between 0 and 0.60 m s^{-1}. For sensible heat flux, our algorithm has an absolute error of about 6 W m^{-2} (i.e. typically RMSE/$\sqrt{2}$ from Table III) and seems to be biased low by 2–4 W m^{-2}. Finally, for predicting the latent heat flux, our algorithm has an absolute error of only 3.5 W m^{-2} and a bias error of only 0.05 W m^{-2}.

In closing, we have developed FORTRAN code for the bulk flux algorithm that we have described here. It complements the related algorithm that Andreas *et al.* (2010) reported for winter sea ice. We are willing to share the code for both algorithms with anyone interested in trying it out.

Acknowledgements

The US National Science Foundation (NSF) supported our initial participation in SHEBA with awards to the US Army Cold Regions Research and Engineering Laboratory, NOAA's Environmental Technology Laboratory (now the Earth System Research Laboratory), the Naval Postgraduate School, and the Cooperative Institute for Research in Environmental Sciences. NSF also supported our use of the Flux-PAM stations from the facilities pool at the National Center for Atmospheric Research. Both NSF (award 06-11942) and the National Aeronautics and Space Administration (award NNX07AL77G) supported ELA at NorthWest Research Associates during the preparation of this manuscript, and NSF also supported POGP with award 06-12428. We thank Donald K. Perovich for providing his data on lead and melt pond coverage during SHEBA and Thomas C. Grenfell for his related measurements of surface water temperature in these features. Finally, we thank Timo Vihma and an anonymous reviewer for helpful comments on an earlier version of the manuscript.

References

Anderson RJ. 1987. Wind stress measurements over rough ice during the 1984 Marginal Ice Zone Experiment. *J. Geophys. Res.* **92**(C7): 6933–6941.

Andreas EL. 1987. A theory for the scalar roughness and the scalar transfer coefficients over snow and sea ice. *Boundary-Layer Meteorol.* **38**: 159–184.

Andreas EL. 1995. Air–ice drag coefficients in the western Weddell Sea. 2: A model based on form drag and drifting snow. *J. Geophys. Res.* **100**(C3): 4833–4843.

Andreas EL. 1998. The atmospheric boundary layer over polar marine surfaces. Pp 715–773 in *Physics of ice-covered seas*, Vol. 2, Leppäranta M (ed). Helsinki University Press.

Andreas EL. 2002. Parameterizing scalar transfer over snow and ice: A review. *J. Hydrometeorol.* **3**: 417–432.

Andreas EL. 2005. '*Handbook of physical constants and functions for use in atmospheric boundary layer studies.*' ERDC/CRREL Monogr. No. M-05-01, 42 pp. US Army Cold Regions Research and Engineering Laboratory: Hanover, New Hampshire.

Andreas EL, Emanuel KA. 2001. Effects of sea spray on tropical cyclone intensity. *J. Atmos. Sci.* **58**: 3741–3751.

Andreas EL, Makshtas AP. 1985. Energy exchange over Antarctic sea ice in the spring. *J. Geophys. Res.* **90**(C4): 7199–7212.

Andreas EL, Tucker WB III, Ackley SF. 1984. Atmospheric boundary-layer modification, drag coefficient, and surface heat flux in the Antarctic marginal ice zone. *J. Geophys. Res.* **89**(C1): 649–661.

Andreas EL, Fairall CW, Guest PS, Persson POG. 1999. 'An overview of the SHEBA atmospheric surface flux program.' Pp 411–416 in *Proceedings of Fifth Conference on polar meteorology and oceanography*, Dallas, Texas, 10–15 January 1999. American Meteorological Society: Boston.

Andreas EL, Guest PS, Persson POG, Fairall CW, Horst TW, Moritz RE, Semmer SR. 2002. Near-surface water vapor over polar sea ice is always near ice saturation. *J. Geophys. Res.* **107**: 8033, DOI: 10.1029/2000JC000411.

Andreas EL, Fairall CW, Grachev AA, Guest PS, Horst TW, Jordan RE, Persson POG. 2003. 'Turbulent transfer coefficients and roughness lengths over sea ice: The SHEBA results.' Paper 3.11 in *Proceedings of 7th Conference on polar meteorology and oceanography*, Hyannis, Massachusetts, 12–16 May 2003. American Meteorological Society: Boston.

Andreas EL, Jordan RE, Makshtas AP. 2004. Simulations of snow, ice, and near-surface atmospheric processes on Ice Station Weddell. *J. Hydrometeorol.* **5**: 611–624.

Andreas EL, Jordan RE, Makshtas AP. 2005a. Parameterizing turbulent exchange over sea ice: The Ice Station Weddell results. *Boundary-Layer Meteorol.* **114**: 439–460.

Andreas EL, Persson POG, Jordan RE, Horst TW, Guest PS, Grachev AA, Fairall CW. 2005b. 'Parameterizing the turbulent surface fluxes over summer sea ice.' Paper J1.15 in *Proceedings of 8th Conference on polar meteorology and oceanography*, San Diego, California, 9–13 January 2005. American Meteorological Society: Boston.

Andreas EL, Claffey KJ, Jordan RE, Fairall CW, Guest PS, Persson POG, Grachev AA. 2006. Evaluations of the von Kármán constant in the atmospheric surface layer. *J. Fluid Mech.* **559**: 117–149.

Andreas EL, Persson POG, Hare JE. 2008. A bulk turbulent air–sea flux algorithm for high-wind, spray conditions. *J. Phys. Oceanogr.* **38**: 1581–1596.

Andreas EL, Persson POG, Jordan RE, Horst TW, Guest PS, Grachev AA, Fairall CW. 2010. Parameterizing turbulent exchange over sea ice in winter. *J. Hydrometeorol.* **11**: 87–104.

Arya SPS. 1975. A drag partition theory for determining the large-scale roughness parameter and wind stress on the Arctic pack ice. *J. Geophys. Res.* **80**(24): 3447–3454.

Banke EG, Smith SD, Anderson RJ. 1980. Drag coefficients at AIDJEX from sonic anemometer measurements. Pp 430–442 in *Sea ice processes and models*, Pritchard RS (ed). University of Washington Press: Seattle.

Birnbaum G, Lüpkes C. 2002. A new parameterization of surface drag in the marginal sea ice zone. *Tellus* **54A**: 107–123.

Bradley RS, Keimig FT, Diaz HF. 1993. Recent changes in the North American Arctic boundary layer in winter. *J. Geophys. Res.* **98**(D5): 8851–8858.

Briegleb BP, Bitz CM, Hunke EC, Lipscomb WH, Holland MM, Schramm JL, Moritz RE. 2004. '*Scientific description of the sea ice component in the Community Climate System Model, version three.*' NCAR Tech. Note NCAR/TN-463+STR, 70 pp. National Center for Atmospheric Research: Boulder, Colorado.

Brunke MA, Zhou M, Zeng X, Andreas EL. 2006. An intercomparison of bulk aerodynamic algorithms used over sea ice with data from the Surface Heat Budget for the Arctic Ocean (SHEBA) experiment. *J. Geophys. Res.* **111**: C09001, DOI: 10.1029/2005JC002907.

Brutsaert W. 1982. *Evaporation into the atmosphere: Theory, history, and applications*. D. Reidel: Dordrecht.

Claffey KJ, Andreas EL, Perovich DK, Fairall CW, Guest PS, Persson POG. 1999. 'Surface temperature measurements at SHEBA.' Pp 327–332 in *Proceedings of Fifth Conference on polar meteorology and oceanography*, Dallas, Texas, 10–15 January 1999. American Meteorological Society: Boston.

Collins WD, Bitz CM, Blackmon ML, Bonan GB, Bretherton CS, Carton JA, Chang P, Doney SC, Hack JJ, Henderson TB, Kiehl JT, Large WG, McKenna DS, Santer BD, Smith RD. 2006. The Community Climate System Model version 3 (CCSM3). *J. Climate* **19**: 2122–2143.

Deardorff JW. 1970. Convective velocity and temperature scales for the unstable planetary boundary layer and for Rayleigh convection. *J. Atmos. Sci.* **27**: 1211–1213.

Denby B, Snellen H. 2002. A comparison of surface renewal theory with the observed roughness length for temperature on a melting glacier surface. *Boundary-Layer Meteorol.* **103**: 459–468.

Dozier J, Warren SG. 1982. Effect of viewing angle on the infrared brightness temperature of snow. *Water Resour. Res.* **18**: 1424–1434.

Ebert EE, Curry JA. 1993. An intermediate one-dimensional thermodynamic sea ice model for investigating ice–atmosphere interactions. *J. Geophys. Res.* **98**(C6): 10085–10109.

Fairall CW, Bradley EF, Rogers DP, Edson JB, Young GS. 1996. Bulk parameterization of air–sea fluxes for Tropical Ocean–Global Atmosphere Coupled–Ocean Atmosphere Response Experiment. *J. Geophys. Res.* **101**(C2): 3747–3764.

Fairall CW, Persson POG, Bradley EF, Payne RE, Anderson SP. 1998. A new look at calibration and use of Eppley precision infrared radiometers. Part I: Theory and application. *J. Atmos. Oceanic Technol.* **15**: 1229–1242.

Fairall CW, Bradley EF, Hare JE, Grachev AA, Edson JB. 2003. Bulk parameterization of air–sea fluxes: Updates and verification for the COARE algorithm. *J. Climate* **16**: 571–591.

Garratt JR. 1992. *The atmospheric boundary layer*. Cambridge University Press.

Garratt JR, Hicks BB. 1973. Momentum, heat and water vapour transfer to and from natural and artificial surfaces. *Q. J. R. Meteorol. Soc.* **99**: 680–687.

Godfrey JS, Beljaars ACM. 1991. On the turbulent fluxes of buoyancy, heat and moisture at the air–sea interface at low wind speeds. *J. Geophys. Res.* **96**(C12): 22043–22048.

Grachev AA, Fairall CW, Persson POG, Andreas EL, Guest PS. 2005. Stable boundary-layer scaling regimes: The SHEBA data. *Boundary-Layer Meteorol.* **116**: 201–235.

Grachev AA, Andreas EL, Fairall CW, Guest PS, Persson POG. 2007a. SHEBA flux-profile relationships in the stable atmospheric boundary layer. *Boundary-Layer Meteorol.* **124**: 315–333.

Grachev AA, Andreas EL, Fairall CW, Guest PS, Persson POG. 2007b. On the turbulent Prandtl number in the stable atmospheric surface layer. *Boundary-Layer Meteorol.* **125**: 329–341.

Guest PS, Davidson KL. 1987. The effect of observed ice conditions on the drag coefficient in the summer East Greenland Sea marginal ice zone. *J. Geophys. Res.* **92**(C7): 6943–6954.

Guest PS, Davidson KL. 1991. The aerodynamic roughness of different types of sea ice. *J. Geophys. Res.* **96**(C3): 4709–4721.

Hartmann J, Kottmeier C, Wamser C, Augstein E. 1994. Aircraft measured atmospheric momentum, heat and radiation fluxes over Arctic sea ice. Pp 443–454 in *The polar oceans and their role in shaping global environment*, Johannessen OM, Muench RD, Overland JE (eds). *Geophys. Monogr.* 85. American Geophysical Union: Washington, DC.

Holland MM, Bitz CM, Hunke EC, Lipscomb WH, Schramm JL. 2006. Influence of the sea ice thickness distribution on polar climate in CCSM3. *J. Climate* **19**: 2398–2414.

Holtslag AAM, De Bruin HAR. 1988. Applied modeling of the nighttime surface energy balance over land. *J. Appl. Meteorol.* **27**: 689–704.

Horst TW, Oncley SP, Semmer SR. 1997. 'Measurement of water vapor fluxes using capacitance RH sensors and cospectral similarity.' Pp 360–361 in *Proceedings of 12th Symposium on boundary layers and turbulence*, Vancouver, British Columbia, 28 July–1 August 1997. American Meteorological Society: Boston.

Hunke EC, Lipscomb WH. 2008. '*CICE: The Los Alamos sea ice model, documentation and software user's manual, version 4.0.*' Tech. Rep. LA-CC-06-012, 59 pp. Los Alamos National Laboratory: Los Alamos, New Mexico.

Huwald H, Tremblay L-B, Blatter H. 2005. Reconciling different observational data sets from Surface Heat Budget of the Arctic Ocean (SHEBA) for model validation purposes. *J. Geophys. Res.* **110**: C05009, DOI: 10.1029/2003JC002221.

Intrieri JM, Fairall CW, Shupe MD, Persson POG, Andreas EL, Guest PS, Moritz RE. 2002. An annual cycle of Arctic surface cloud forcing at SHEBA. *J. Geophys. Res.* **107**: 8039, DOI: 10.1029/2000JC000439.

Jordan RE, Andreas EL, Makshtas AP. 1999. Heat budget of snow-covered sea ice at North Pole 4. *J. Geophys. Res.* **104**(C4): 7785–7806.

Kahl JD. 1990. Characteristics of the low-level temperature inversion along the Alaskan Arctic coast. *Int. J. Climatol.* **10**: 537–548.

Kaimal JC, Finnigan JJ. 1994. *Atmospheric boundary layer flows: Their structure and measurement.* Oxford University Press: New York.

Kaimal JC, Gaynor JE. 1991. Another look at sonic thermometry. *Boundary-Layer Meteorol.* **56**: 401–410.

Kiehl JT, Gent PR. 2004. The Community Climate System Model, version 2. *J. Climate* **17**: 3666–3682.

Larsen SE, Edson JB, Fairall CW, Mestayer PG. 1993. Measurement of temperature spectra by a sonic anemometer. *J. Atmos. Oceanic Technol.* **10**: 345–354.

Launiainen J, Vihma T. 1990. Derivation of turbulent surface fluxes – An iterative flux-profile method allowing arbitrary observing heights. *Environ. Software* **5**: 113–124.

Liu WT, Katsaros KB, Businger JA. 1979. Bulk parameterization of air–sea exchanges of heat and water vapor including the molecular constraints at the interface. *J. Atmos. Sci.* **36**: 1722–1735.

Lüpkes C, Birnbaum G. 2005. Surface drag in the Arctic marginal sea-ice zone: A comparison of different parameterisation concepts. *Boundary-Layer Meteorol.* **117**: 179–211.

MacDonald RW, Griffiths RF, Hall DJ. 1998. An improved method for the estimation of surface roughness of obstacle arrays. *Atmos. Environ.* **32**: 1857–1864.

Mahrt L. 1998. Stratified atmospheric boundary layers and breakdown of models. *Theor. Comput. Fluid Dyn.* **11**: 263–279.

Mahrt L. 1999. Stratified atmospheric boundary layers. *Boundary-Layer Meteorol.* **90**: 375–396.

Mahrt L. 2008. Bulk formulation of surface fluxes extended to weak-wind stable conditions. *Q. J. R. Meteorol. Soc.* **134**: 1–10.

Mai S, Wamser C, Kottmeier C. 1996. Geometric and aerodynamic roughness of sea ice. *Boundary-Layer Meteorol.* **77**: 233–248.

Marshall JK. 1971. Drag measurements in roughness arrays of varying density and distribution. *Agric. Meteorol.* **8**: 269–292.

Maykut GA. 1978. Energy exchange over young sea ice in the central Arctic. *J. Geophys. Res.* **83**(C7): 3646–3658.

Militzer JM, Michaelis MC, Semmer SR, Norris KS, Horst TW, Oncley SP, Delany AC, Brock FV. 1995. 'Development of the prototype PAM III/Flux-PAM surface meteorological station.' Pp 490–494 in *Proceedings of 9th Symposium on meteorological observations and instrumentation*, Charlotte, North Carolina, 27–31 March 1995. American Meteorological Society: Boston.

Overland JE. 1985. Atmospheric boundary layer structure and drag coefficients over sea ice. *J. Geophys. Res.* **90**(C5): 9029–9049.
Overland JE, McNutt SL, Groves J, Salo S, Andreas EL, Persson POG. 2000. Regional sensible and radiative heat flux estimates for the winter Arctic during the Surface Heat Budget of the Arctic Ocean (SHEBA) experiment. *J. Geophys. Res.* **105**(C6): 14093–14102.
Paulson CA. 1970. The mathematical representation of wind speed and temperature profiles in the unstable atmospheric surface layer. *J. Appl. Meteorol.* **9**: 857–861.
Perovich DK, Tucker WB III, Ligett KA. 2002. Aerial observations of the evolution of ice surface conditions during summer. *J. Geophys. Res.* **107**: 8048, DOI: 10.1029/2000JC000449.
Persson POG, Fairall CW, Andreas EL, Guest PS, Perovich DK. 2002. Measurements near the Atmospheric Surface Flux Group tower at SHEBA: Near-surface conditions and surface energy budget. *J. Geophys. Res.* **107**: 8045, DOI: 10.1029/2000JC000705.
Raupach MR. 1992. Drag and drag partition on rough surfaces. *Boundary-Layer Meteorol.* **60**: 375–395.
Raupach MR, Thom AS, Edwards I. 1980. A wind-tunnel study of turbulent flow close to regularly arrayed rough surfaces. *Boundary-Layer Meteorol.* **18**: 373–397.
Reijmer CH, Van Meijgaard E, Van den Broeke MR. 2004. Numerical studies with a regional atmospheric climate model based on changes in the roughness length for momentum and heat over Antarctica. *Boundary-Layer Meteorol.* **111**: 313–337.
Schotanus P, Nieuwstadt FTM, De Bruin HAR. 1983. Temperature measurement with a sonic anemometer and its application to heat and moisture fluxes. *Boundary-Layer Meteorol.* **26**: 81–93.
Serreze MC, Kahl JD, Schnell RC. 1992. Low-level temperature inversions of the Eurasian Arctic and comparisons with Soviet drifting station data. *J. Climate* **5**: 615–629.
Shao Y, Yang Y. 2005. A scheme for drag partition over rough surfaces. *Atmos. Environ.* **39**: 7351–7361.
Smeets CJPP, Van den Broeke MR. 2008. The parameterisation of scalar transfer over rough ice. *Boundary-Layer Meteorol.* **128**: 339–355.
Smeets CJPP, Duynkerke PG, Vugts HF. 1998. Turbulence characteristics of the stable boundary layer over a mid-latitude glacier. Part I: A combination of katabatic and large-scale forcing. *Boundary-Layer Meteorol.* **87**: 117–145.
Tjernström M, Graversen RG. 2009. The vertical structure of the lower Arctic troposphere analysed from observations and the ERA-40 reanalysis. *Q. J. R. Meteorol. Soc.* **135**: 431–443.
Uttal T, Curry JA, McPhee MG, Perovich DK, Moritz RE, Maslanik JA, Guest PS, Stern HL, Moore JA, Turenne R, Heiberg A, Serreze MC, Wylie DP, Persson POG, Paulson CA, Halle C, Morison JH, Wheeler PA, Makshtas A, Welch H, Shupe MD, Intrieri JM, Stamnes K, Lindsey RW, Pinkel R, Pegau WS, Stanton TP, Grenfeld TC. 2002. Surface Heat Budget of the Arctic Ocean. *Bull. Am. Meteorol. Soc.* **83**: 255–275.
Vickers D, Mahrt L. 2006. Evaluation of the air–sea bulk formula and sea-surface temperature variability from observations. *J. Geophys. Res.* **111**: C05002, DOI: 10.1029/2005JC003323.
Vihma T. 1995. Subgrid parameterization of surface heat and momentum fluxes over polar oceans. *J. Geophys. Res.* **100**(C11): 22625–22646.
Warren SG. 1982. Optical properties of snow. *Rev. Geophys. Space Phys.* **20**: 67–89.
Wilks DS. 2006. *Statistical methods in the atmospheric sciences*, 2nd edition. Academic Press: Amsterdam.
Willmott CJ. 1982. Some comments on the evaluation of model performance. *Bull. Am. Meteorol. Soc.* **63**: 1309–1313.
Wooding RA, Bradley EF, Marshall JK. 1973. Drag due to regular arrays of roughness elements of varying geometry. *Boundary-Layer Meteorol.* **5**: 285–308.
Zeng X, Zhao M, Dickinson RE. 1998. Intercomparison of bulk aerodynamic algorithms for the computation of sea surface fluxes using TOGA COARE and TAO data. *J. Climate* **11**: 2628–2644.

